Benchmark exercise for multi-dimensional thermohydraulic analysis codes

—Buoyancy driven penetration flow phenomena and thermal stratification—

March, 1996

O-arai Engineering Center
Power Reactor and Nuclear Fuel Development Corporation

Ⓝ

多次元熱流動解析コードの国際ベンチマーク
-浮力による潜り込み現象と温度成層化現象について-

上出　英樹[*1]、家田　芳明[*2]、小林　順[*1]、二ノ方　寿[*3]

要旨

高速炉の熱流動の分野においてベンチマーク実験を行ない、これに対する多次元熱流動解析コードの国際ベンチマークを実施した。合計１２種類の熱流動解析手法が、浮力による潜り込み現象並びに温度成層化現象を対象とするベンチマークに適用された。解析手法として有限差分法、有限要素法、及びその乱流モデル、対流項の高次差分解法の現象に対する適用性を検討した、有限差分法では乱流モデルと高次差分法を組み合わせた手法が高い適用性を示した。また、有限要素法についても乱流モデルの重要性が明かとなった。解析手法の検討を通して潜り込み現象、温度成層化現象を解析する上で、低乱流状態で浮力の影響を受ける混合対流条件下の流れに対する乱流モデルの開発が重要であることが示された。なお、本ベンチマークは国際水理学会（IAHR）の第７回新型炉熱流動ワーキンググループの会合（1992年8月、於ドイツ、カールスルーエ）のために準備したものである。

*1　安全工学部原子炉工学室
*2　安全工学部原子炉工学室（現在、基盤技術部、熱流体技術開発室）
*3　安全工学部（現在、東京工業大学、原子炉工学研究所）

I

Benchmark exercise for multi-dimensional thermohydraulic analysis codes
- Buoyancy driven penetration flow phenomena and thermal stratification -

H. Kamide[*1], Y. Ieda[*2], J. Kobayashi[*1], and H. Ninokata[*3]

ABSTRACT

A benchmark exercise for multi-dimensional thermohydraulic codes was carried out related to natural convection decay heat removal in liquid metal-cooled fast breeder reactors. A total of twelve computational methods were applied to the benchmark problem which simulated mixed forced and buoyancy driven penetration flow and thermal stratification phenomena. The applicability of turbulence models and higher order schemes of convection terms, was examined, and a combined method incorporating a higher order scheme and a turbulence model was found to be highly effective among the group of finite difference methods. The importance of turbulence models was also recognized for the finite element method. Development of a turbulence model applicable to the mixed convection flow regime was also discussed.

*1 Safety Engineering Division, Reactor Engineering Section
*2 Advanced Technology Division, Thermal-hydraulics Reserch Section
*3 Present address: Research Laboratory for Nuclear Reactors, Tokyo Institute of
   Technology, 2-12-1 Ohokayama, Meguro-ku, Tokyo 152, Japan

CONTENTS

List of Tables

List of Figures

1. Introduction

A benchmark exercise for multi-dimensional thermohydraulic codes was carried out in the field of liquid metal-cooled fast breeder reactors. The primary purpose of the exercise was to determine the characteristics and applicability of the finite difference method/finite element method, turbulence models, and higher order schemes of convection terms for a mixed convection flow, i.e., natural circulation. This benchmark exercise was prepared for the seventh meeting of the IAHR working group on Advanced Nuclear Reactors Thermal Hydraulics, held at Karlsruhe, Germany, on August 28-30, 1991[1].

A series of benchmark experiments was performed to investigate thermal stratification and plenum-core thermohydraulic interactions of a fast reactor under natural circulation conditions. While the decay heat is removed by heat exchangers installed in an upper plenum of a reactor vessel, i.e., by immersed coolers, the cold fluid coming from the cooler normally induces thermal stratification in the plenum. Under certain conditions, this cold fluid penetrates into lower power subassemblies in a core. Such phenomena were observed in water experiments[2], [3] simulating the scram transient of a loop-type and a pool-type reactor and also were investigated using a vertical rod bundle channel connected to a cooled plenum[4].

In the benchmark experiment, the reactor core, the upper plenum, and the immersed cooler were modeled using a simple apparatus. The cold fluid penetration into the simulated core was observed under certain conditions. A number of parameter experiments were carried out to determine the onset condition of this penetration flow.

Four cases were selected among these parameter experiments for use as the benchmark problem. The benchmark analyses were performed as a blind test; i.e., only the boundary conditions of the above experiments were provided to those participating in the exercise. A total of 12 thermohydraulic analysis methods were applied to the benchmark exercise. The participants were from Germany, Italy, and Japan. Applicability of various computational methods, e.g., turbulence models and higher order schemes, was discussed for the mixed convection flow and the penetration flow.

2. Benchmark Experiment

2.1 Experimental Setup

The experimental model was composed of an abstract of an upper neutron shielding part of a reactor core and an upper plenum. Figure 1 shows the test section which is a slab geometry model 150 mm in depth with water as the working fluid. In the experimental model, an upper neutron shield of a fuel subassembly was represented by a simple rectangular inlet channel, a hot plenum and an immersed cooler by the plenum and the cold wall. The ceiling of the plenum section was inclined intentionally to check for adequate boundary treatment in the computational procedure.

Hot fluid was supplied to the plenum from the inlet channel and flowed through the plenum toward the outlet. The flow rate and the inlet temperature were kept constant. A large clockwise recirculating flow was observed in the plenum. The fluid cooled by the cold wall flowed back toward the exit of the inlet channel, forming a stratified flow at the bottom of the plenum. This cold fluid flow interacted and mixed with the hot fluid flowing upward from the inlet channel. Cold fluid penetration into the inlet channel was observed under certain conditions.

The lower part of the inlet channel had a flow straightener 500 mm in length. The velocity distribution was found to be almost uniform at the outlet of the flow straightener. The velocity distribution developed in the plain rectangular channel 1500 mm in length which is situated after the flow straightener.

A cooling box was attached to the cold wall of the plenum test section. The cold wall was made of a copper plate 5 mm in thickness. Cold water of the secondary loop flowed upward in the cooling box in zigzag directions due to the presence of baffle plates. The flow rate and the inlet temperature were kept constant.

The Cartesian coordinates are defined in Fig. 2. The x-, y-, and z-components of velocity are v_x, v_y, and v_z, respectively. Gravity acts in the z-direction.

Figure 3 shows the temperature measuring points in the test section. Four vertical traverse lines were set in the plenum: P1, P2, P3, and P4. A traverse thermocouple set was installed in the inlet channel. Temperatures were measured in the x-z plane (y = 0 mm) by the Copper-Constantan thermocouples 1 mm in diameter. The data sampling time was 300 seconds with a sampling interval of 0.5 seconds. The averaged temperatures for each 300-second sample were used as the measured results. The measurement accuracy was within 0.15 °C.

The velocity distribution was measured by a probe-type two-dimensional Laser Doppler Anemometer (LDA). The probe of the LDA was traversed by a computer controlled x-y-z traverse unit. The traverse position was accurate to within 0.2 mm. Average velocities of 500 sampled data per position were used. It took 5 to 20 minutes to measure the 500 velocity data per position.

2.2 Experimental Parameters

It is considered that the cold penetration phenomenon into the inlet channel depends on the local temperature difference between the upward hot flow in the channel and the cold fluid in the plenum, and on the upflow velocity in the channel. Thus, the following three parameters were varied to determine the onset and depth of the penetration flow:
   Inlet temperature of the test section: from 20 to 50 °C;
   Flow rate into the test section: from 13.5 to 45 l/min; and
   Inlet temperature of the cooling box: from 10 to 30 °C.

The temperature deviations of the inlet flow into the test section and the cooling box were both within 0.2 °C. The deviation of the inlet flow rate of the test section was below 0.1 l/min. The heat loss from the surrounding walls was no more than 5% of the removal heat of the cooling box (the test section was insulated using a styrene foam plate 5 cm in thickness).

Four test cases, Case 1, 2, 3, and 4, were selected as the benchmark problems from the parameter experiments. The flow rate into the inlet channel was increased in ascending order from Case 1 to Case 4 while all other conditions were kept constant. In Case 1, penetration flow was observed. In Case 4, the forced flow into the test section was 2.5 times larger than that of Case 1 and penetration flow was not observed. The experimental conditions of Cases 1 to 4 are shown in Table 1. In the next section, experimental results of these four cases are discussed.

2.3 Results of Plenum Thermohydraulics

Figure 4 shows the measured velocity fields in the plenum in the x-z plane (y = 0 mm) for Cases 1 and 4. In Case 1, a main flow path was seen along the left wall and the inclined top walls. A large clockwise recirculating flow appeared at the upper right section. A thin film (< 1 cm) downflow stream was observed along the cold wall and a

thin flow toward the exit of the inlet channel along the bottom plate. This is a stratified flow coming from the cold wall. The flow pattern in Case 4 was almost the same as in Case 1. However, the recirculating flow region in Case 4 was shifted to the lower part of the plenum as compared with Case 1.

Vertical distributions of the x-component flow velocity (v_x) and the temperature in Case 1 are shown in Figs. 5 to 8 along the traverse lines P1 to P4, respectively. The characteristics of the plenum thermohydraulics are discussed below based on these profiles and also compared with the calculated results in the next section.

Temperature profiles of Figs. 5 to 7 show a constant temperature region above 250 mm and thermal stratification below this level. Figure 5 shows a leftward flow (negative value) below 150 mm (in the stratified layer).

The temperature distributions across the stratified layer in Figs. 5 to 7 indicated a point around 60 mm where the temperature gradient changed from low to high. This change of the temperature gradient resulted from the mixing at the stratification interface. The standard deviation of the temperatures is shown in Fig. 9 based on the data registered over the 300-second sampling time along the P1 line with the temperature and velocity profiles. The temperature deviation increased above the height of the point where the gradient changed (z=60 to 80 mm), indicating that greater mixing occurred in this region. The velocity profile showed a larger gradient in this region than in the lower region. These data suggest that turbulence mixing due to shear stress would influence the velocity and temperature profiles.

The P3 line crossed the recirculation flow region in the plenum. Thus, the velocity profile along the P3 line showed extension of the recirculation flow into the stratified layer (Fig. 7). The recirculation flow was observed above the height of 200 mm, the stratified flow below the level of 80 mm and a quiescent region in the middle.

Flow along the inclined top wall was registered along the P2 line (see Fig. 6). The increase in v_x between 550 and 620 mm (5 mm below the top wall) was linear. The velocity decrease due to the wall shear stress could not be measured due to its proximity to the wall.

The v_x and temperature distributions in Case 4 along the P1 to P4 lines are shown in Figs. 10 to 13. The flow rate into the inlet channel was 2.5 times larger in Case 4 than that in Case 1. The v_x at 600 mm along the P2 line (Fig. 11) was larger than Case 1 by a factor of 2. This means that the main flow was influenced strongly by the forced flow through the inlet channel. In contrast, the maximum velocity of the stratified flow along the bottom plate was about 1 cm/sec in Case 4, nearly the same as Case 1.

The recirculating flow extended above 100 mm, as shown in Fig. 12, and this lower end position was 100 mm lower than that of Case 1 (see Fig. 7). These differences in the plenum thermohydraulics were the result of the inertia of the main flow being larger in Case 4 than Case 1 while the heat removal from the cold wall was approximately the same. Numerical simulations of Cases 1 and 4 made it, therefore, possible to see the effects of the inertia of main flow on the cold stratified flow.

2.4 Results of Penetration Flow

The buoyancy driven penetration flow into the inlet channel was detected in Cases 1, 2, and 3. No penetration flow was observed in Case 4. The lower flow rate in the inlet channel resulted in penetration flow. It is easily predicted that the velocity profile in the channel is also important for penetration flow. In Fig. 14, velocity profiles (v_z-component) in the x-direction are shown at a depth of 200 mm (z = -200 mm) for Cases 1 to 4 without any flow in the cooling box (homogeneous temperature condition). The

resultant velocity profiles showed characteristics of the turbulent flow described by the logarithmic law.

The penetration flow in Case 1 was visualized by a laser light sheet and by a neutrally buoyant dye injection. Figure 15 illustrates the flow pattern. Photo A is a front view and B is a left-sided view. Photo A shows a typical penetration flow and photo B shows several falling flows observed along the bottom plate, indicating that the film flows tended to traverse down along the specific flow paths from the corner edge, once penetration was triggered. The flow in each path was in a thin film, about 10 mm wide in the y-direction and typically a few mm thick in the x-direction. The penetration phenomena were not stable; i.e., the penetration depth varied with time from 0 cm to a few cm and back to 0 cm and this cycle was repeated. Time period of each penetration cycle was typically a few seconds.

The penetration was detected by changes in temperature in the inlet channel using the thermocouple set (see Fig. 3). The thermocouple set could traverse in the z-direction in the x-z plane (y = 0 mm). The measured temperatures are shown in Fig. 16 for Case 1 at a depth of 10 mm (z = -10 mm). The temperature at the right end position (x = 49 mm) showed the largest fluctuations. This is consistent with the visualized flow pattern; the penetration flow formed thin films along the right side wall of the inlet channel.

The frequency of penetration flow was obtained by evaluating the temperature history of the right end thermocouple; there were steep spiked-shaped dips going down from the temperature at the channel inlet (48.9 °C). Each spike corresponded to one penetration flow. The obtained frequency of the penetration flow in Case 1 is shown in Fig. 17. The frequency decreased as the thermocouple was moved deeper into the inlet channel. From this figure, we defined the maximum penetration depth and the occurrence of penetration flow as follows:

Penetration flow was considered to have occurred when the flow was detected with at least a frequency of 1/1000 cps at z= -1 cm and,

Maximum penetration depth is the deepest position where the penetration flow was detected with at least a frequency of 1/1000 cps.

Here the frequency of 1/1000 cps was defined as the minimum cps which could be detected (>100 counts) over a 24-hour period. Counts detected at a lower frequency were not included in the statistical analysis.

A total of 30 cases were carried out to obtain the onset condition of the penetration flow and the maximum depth. Figure 18 shows a map of the penetration flow with respect to the Reynolds number, Re, and the Grashof number, Gr. The circles and crosses in the figure represent cases where the penetration flow did and did not occur, respectively. The definitions of Re and Gr numbers are:

$Re = v_z D / v$,

$Gr = g \beta \Delta T D^3 / v^2$,

Figure 18 depicts the two regions separated by the straight line $Gr/Re^2 = 0.55$: Penetration flows were observed in the upper left region but not in the lower right. Thus, the onset condition of the penetration flow was that Gr/Re^2 becomes larger than a critical value, which was constant in a turbulent flow regime in the channel (3000 < Re < 10000). The positions of Cases 1 to 4 are also shown in this figure.

Modi and Torrance[5] experimentally and numerically examined the flow penetration process in a vertical duct with air. They reported that the onset of penetration flow was represented as Gr/Re^2 increased over a critical value (between 0.50 and 0.71) in a turbulent flow regime (Re $\approx$ 3000). The results of our experiment using water were in good agreement with this air experiment.

Penetration flow of water was investigated by Barakat and Todreas[6]. They examined the penetration of cold water into hot upflowing annular channels with different outer diameters; the channels were heated by a centrally positioned heater rod. The penetration depth was correlated with Gr/Re based on the assumption that the wall shear force would play an important role in the penetration process. It was also reported that the onset condition of penetration was dependent on Gr/Re.

The onset points of the penetration flow obtained by Barakat are replotted in log-log axes of Re and Gr, as shown in Fig. 19. This figure shows that the onset data of Barakat were also on the straight lines of Gr/Re^2 = constant in low Re flow (80 < Re < 400) condition.

Jerng and Todreas[4] experimentally and numerically examined the penetration flow into vertical heater pin bundles below a non-heated shield section using water as a working fluid. They reported that Gr/Re^2 was related both to onset and depth of penetration. The energy exchange between the penetrating and forced flow was identified as a key mechanism controlling the depth of penetration.

The maximum penetration depths in the present study are shown in Fig. 20 with respect to Gr/Re^2. The maximum depth had a tendency to increase with Gr/Re^2. However, a large diversity was also found. Figure 21 shows the contour of depth on the Gr/Re^2 and 1/Re axes. The penetration depth made a smooth surface; when the Gr/Re^2 value remained constant, the penetration depth increased with the value of 1/Re. This Re dependency is the result of turbulent mixing and shear flow mixing between cold penetration flow and hot upflow; higher mixing (higher Re) remains at a shallow depth due to a decrease in the negative buoyancy force and an increase in shear stress.

From the present study and the current literature, the onset condition of the buoyancy induced penetration flow which occurs when Gr/Re^2 exceeds a critical value applies not only to air but to water under a wide range of Re values, although the critical value is dependent on the channel geometry and the working fluid. The penetration depth was correlated not only to Gr/Re^2 but also to Re.

3. Benchmark Problem

3.1 Benchmark Problem and Two-Dimensional Model Assumption

The benchmark exercise was carried out to clarify applicability to thermal stratification in the plenum and buoyancy induced penetration flow into the inlet channel. The exercise was a blind test, i.e., only the boundary conditions of the experiments were described in the benchmark problem. The problem required participants to provide the profiles of the temperature and v_x in the plenum along the P1 to P4 lines, occurrence of the penetration flow, and its maximum depth in Cases 1 to 4.

To facilitate the benchmark calculations some of the measured data were provided as control results. This information was used to check the calculations while participants conducted preliminary calculations to determine the mesh arrangement.

The simulation geometry was set in two dimensions. In reality, the thermal hydraulic phenomena occurring in the test section showed a three-dimensional behavior if examined closely. However, we assumed only two dimensions in a limited mid-region in the y-direction. The profile of v_z in the y-direction in the inlet channel was almost flat in the mid-region near y = 0 mm extending to a comparably broad region while the velocities near the wall decreased due to the effect of the wall friction. Therefore, the effect of the wall friction on the velocity field in the mid-region of the inlet channel can be assumed to be negligible in the following discussions. In the same way, the velocity profile in the y-direction was also flat in the mid-region near y = 0 mm in the plenum. The temperature distribution in the y-direction was always flat both in the inlet channel and in the plenum. We therefore analyzed only the velocity and temperature fields on the x-z plane at y = 0 mm.

3.2 Boundary Conditions

The benchmark participants solved the cases using the boundary conditions of the velocity and temperature profile at the inlet channel and the heat transfer data on the cooling wall given below.

Inlet velocity profile
The following two options were prepared.

Option-1
A uniform velocity profile at the outlet of the flow straightener was given as the inlet boundary condition and the development of the velocity profile along the inlet channel was to be calculated by an analysis code. The 1500 mm inlet channel should be sufficiently long to attain a nearly fully developed turbulent flow field in the channel for the experiment and also for the calculation. Additionally, the measured profile of velocity component v_z in the x-direction was provided at y = 0 mm, z = -200 mm as a control result in Fig. 14

Option-2
The measured v_z profile at z = -200 mm, i.e., the control result shown in Fig. 14, was used as the inlet boundary conditions only for Case 4. Fitting curves are as follows.

v_z (cm/sec) = -0.8492 x^2 + 5.6786 x - 0.0233 $\qquad$ (0<x≤3 mm),

v_z (cm/sec) = 1.8195 ln(x) + 7.5229 $\qquad$ (3<x≤25 mm),

v_z (cm/sec) = 1.8195 ln(50-x) + 7.5229 $\qquad$ (25<x≤47 mm), and

v_z (cm/sec) = -0.8492 $(50-x)^2$ + 5.6786 (50-x) - 0.0233 $\qquad$ (47<x<50 mm).

Since the cold penetration flow was not observed in Case 4, the velocity profile near the wall in the inlet channel is less important for Case 4 than for Case 1.

Inlet temperature
The temperature distribution in the inlet channel was uniform in the region where the cold penetration did not take place. Therefore, the point data were given as the inlet temperature.

Heat transfer on the surrounding walls
The heat loss to the ambiance, i.e., the difference between the heat removed from the test section and the heat removed by the cooling box, was no more than 5%. Therefore the surrounding walls, except for the cold wall, were treated as the adiabatic boundaries.

Heat transfer on the cold wall
The temperatures on the surface of the cold wall were measured and total heat removed by the cooling box was calculated based on the inlet and outlet temperatures and the flow rate of the cooling box. Two options were prepared.

Option-1
The wall surface temperatures were used as boundary conditions. In this case, the heat transfer coefficient on the cold wall was not given because it depends on the mesh sizes next to the wall in a multi-dimensional analysis scheme. A participant had to tune the heat transfer coefficient for his mesh arrangement with a given wall temperature and heat flux through the wall. Alternatively, one had to divide the thermal boundary layer into some meshes to avoid using the heat transfer coefficient.

Option-2
The heat flux through the cold wall was given as the boundary condition. The average heat flux through the cold wall was obtained as the total heat removed by the cooling box divided by the surface area of the cold wall. In this description, two-dimensional thermal hydraulic phenomena were assumed in the test section based on the temperature and velocity field in the x-z plane (y = 0 mm). It is noted that the velocities in the x-z plane are not equal to the averaged velocities because the velocity distribution in the y-direction was not accounted for. The heat removed from the cold wall, if we limit ourselves in the x-z plane and to be consistent with the two-dimensional assumption, is not same as the actual average heat flux of the cold wall. The heat flux for the boundary condition, therefore, is approximated and given by the following equation.

$$q'' = (Q/A_c) \, v_{av} / (W/A_{in})$$

Boundary conditions used in the analyses of Cases 1, 2, 3, and 4 are shown in Table 2.

3.3 Control Results

The control results consisted of the profile of the velocity component v_z at z= -200 mm in the inlet channel (see Fig. 14), the temperatures at x= 725 mm, z= 0 mm (see Table 2), and the temperatures and velocity components v_x at z= 25, 125, 250, 375, and 500 mm on the traverse line P1 in Cases 1 and 4 (see Figs. 5 and 10).

4. Applied Methods and Classification

Participants of this benchmark exercise are shown in Table 3. A total of 12 thermohydraulic analysis methods were applied to the benchmark problem. Ten methods were based on the finite difference method (FDM) and two on the finite element method (FEM). In the finite difference method, treatment of the convection terms varied from the first order up-wind to the third order skew up-wind schemes.

Regarding the turbulence models used, the mixing length model, k-ε model, and an algebraic stress/flux model (ASM) proposed by Rodi[7] were incorporated in these methods.

These analysis methods are represented by Method-XYN in the following discussions. X, Y, and N refer to the numerical scheme, turbulence model, and treatment of the convection term, respectively, as follows.

> X   D : a finite difference method,
>   E : a finite element method,
> Y   L : laminar flow model,
>   H : homogeneous turbulent viscosity model,
>   M : mixing length model,
>   K : k-ε model,
>   A : algebraic stress/flux model,

N   1a, b, c : the first order up-wind scheme and a, b, and c denote the
     codes,
     1S : the first order skew up-wind scheme,
     Q : QUICK scheme,
     3 : the third order up-wind scheme, and
     3S : the third order skew up-wind scheme.

All methods applied to the benchmark exercise are listed and classified in Table 4.
Mixing length model incorporated in Method-DM1S is explained in Appendix-1.

Method-DKQ used a modified model constant of k-ε model. The constant C_1 of the
production term in the dissipation rate equation was increased by 15% from the
standard value, which were proposed by Launder and Spalding[8], in order to apply
low Re flows, as shown in Appendix-2. Method-DAQ was carried out by the same
code as Method-DKQ, and the same modified constant (C_1) was used for the
production term in the dissipation rate equation in the algebraic stress/flux model.

5. Calculated Results and Discussion

5.1 Plenum Thermohydraulics

The calculated velocity fields for Case 4, obtained from Method-DL1a, -DL3S, -DKQ,
and -EH, are shown in Fig. 22(a) to (d), respectively. Method-DL1a gave a stable
flow field using the first order up-wind scheme without turbulence models. The flow
field calculated by Method-DKQ was also stable, in which the second order scheme,
QUICK, and the modified k-ε model were incorporated. Method-EH based on the
finite element method used larger viscosity than the molecular viscosity of water by a
factor of 100 to avoid numerical instability. The resultant calculated flow pattern was
stable.

On the other hand, Method-DL3S, in which the third order skew up-wind schemes of
the convection term were incorporated, showed unstable flows where some large eddies
shifted with time. This calculation was performed with a laminar flow assumption for
the entire domain of the analysis.

The flow pattern in the experiment, based on flow visualization, was almost stable.
The angle of the measured velocity vectors at each point in Fig. 4 was nearly constant
over time, e.g., the standard deviation of the velocity angle was only 2.9° at point A in
Case 4. This experimental result means that the calculated unstable flow pattern of
Method-DL3S was not physical. On the other hand, the first order up-wind scheme
gave stable flow without any turbulence models. It produced the unphysical numerical
viscosity which provided a dumping source and stabilized the flow. The third-order
scheme decreased not only the unphysical numerical viscosity but a dumping source as
well.

In Case 4, the Re number was 13,000 in the inlet channel based on the cross section
averaged velocity. Therefore, the flow in the channel was in a turbulent regime. In
other words, the flow field in the plenum had a strong turbulence source at the exit of
the inlet channel. To see the effect of turbulence model on the flow pattern or flow
stability, an additional calculation was carried out by a method with QUICK scheme
and without any turbulence models. Here, the same code with Method-DKQ was used.
The calculated velocity field in Case 4 is shown in Fig. 23. The flow pattern was
unstable and was similar to that of Method-DL3S. A comparison with the result of
Method-DKQ shown in Fig. 22(c) indicated that the stabilizing effect of the k-ε
turbulence model was significant on the flow field.

In the calculations in which the numerical diffusion was reduced by the higher order schemes or the finite element method, the turbulence models or the additional viscosity simulating the turbulent viscosity should be incorporated to avoid the unphysical instability of the global flow field. All the calculated flow patterns agreed with the measured one with respect to the main flow along the left and inclined top walls and the recirculating flow in the upper right region. Details of the plenum thermohydraulics are discussed in following paragraphs.

Distributions of the x-component velocity and temperature along P1 line of Case 1 are compared between experiment and calculations of Method-DL1a and Method-DM1S in Fig. 24. Method-DM1S used the first order skew up-wind scheme for the convection term and the mixing length model as the turbulence model. In this figure, the characteristics of the stratified flow were compared. From the velocity profiles, the width of the stratified flow region in the z-direction was small in Method-DL1a as compared with the experimental results. In Method-DM1S the width was larger than that of Method-DL1a but still smaller than the measured width. The temperature gradient across the thermal stratification of Method-DL1a was much larger than the measured one. In Method-DM1S the temperature distribution showed good agreement with the experimental result.

Figure 25 shows the distributions of the v_x and temperature along the P1 line obtained from Method-DKQ using the modified k-ε model. Here, the effect of this modification is revealed by the comparison with the distributions obtained by an additional calculation using the standard constants of the k-ε model. In the modified k-ε model, the width of the stratified flow region was half of that of the experiment. The temperature distribution agreed well with the measured data. However, in the original k-ε model, the velocity distribution was broad in the stratified flow region and the temperature gradient of the stratified layer was smaller than the experimental result.

Characteristics of the predicted stratified flows were compared among all the applied codes. Half value heights of the stratified flow velocity and the temperature difference across the thermal stratification were selected as the comparison points, as shown in Fig. 26. The comparisons in Fig. 27 show a tendency for the calculations using the turbulence models (Method No. $\geq$ 7) gave better answers. This suggested that the turbulence models played an important role in the prediction of the stratified flow.

Calculated velocity distributions of the recirculating flow and temperature distributions along the P3 line were compared with the measured data. The comparisons for Case 1 and Case 4 are shown in Figs. 28 and 29, respectively. In Case 1, the stratified flow region obtained by Method-DL1a was thinner (z<40 mm) than the experimental result (z<80 mm). Further, bottom of the recirculating flow region calculated by Method-DL1a was lower than the measured data. The temperature distribution across the stratification layer predicted by Method-DL1a had steeper gradient than that of the experiment. On the other hand, the calculated velocity and temperature distributions of Method-DKQ were in good agreement with the measured distributions

In Case 4, the calculated velocity distribution by Method-DL1a showed that the recirculating flow reached the bottom plate. In the temperature profile, the stratified layer was limited in lower level (z<10 mm) due to this enlarged recirculating region. The measured distributions indicated that the recirculating flow region was separated from the stratified flow by a stagnant region and the stratified layer had larger width (200 mm). The calculated distributions by Method-DKQ agreed well with the experimental results.

The maximum v_x and the bottom position of the recirculating flow region were selected for comparison, as shown in Fig. 30. Comparisons of the results of all applied methods are shown in Figs. 31 and 32 for Cases 1 and 4, respectively. The calculations in which the turbulence models were used showed better agreement with the experimental data than the calculations with a laminar flow assumption. This tendency was more apparent in Case 4 than in Case 1. Under the higher velocity condition of recirculation flow, it was difficult to predict the stratified flow using the laminar flow model.

The first order up-wind methods without any turbulence models (like Method-DL1a) showed steep v_x and temperature gradients at the interface between the main recirculation region and the stratified layer. However, the first order up-wind scheme produces numerical diffusion and results in broad distribution, in general. In this benchmark problem, the flow in the stratified region was parallel to the direction of the mesh coordinates. Thus, the numerical diffusions of the momentum and energy in the y-direction were small. This resulted in steep v_x and temperature gradients at the stratification interface for the first order up-wind scheme with a laminar model. The measured distributions of v_x and the temperature suggested that a greater mixing occurred in the stratification interface than the calculations by such simple methods as Method-DL1a.

The turbulence models had significant influences on the stratified flow. The comparison between the original k-ε model and the modified model (Fig. 25) showed that the k-ε model was sensitive to the model constant, C_1 (see Appendix-2). In the algebraic stress/flux model, the same tendency was observed whereby the k-ε model was found to be related to the model constant, C_1. The mixing length model was shown also effective in the prediction of the stratified flow. A procedure to give the mixing length is also important to predict the stratified flow. These results mean that further development of the turbulence model is needed to calculate the stratified flow, which is low Re flow and is governed by buoyancy force.

In order to see the influence of treatment of the inclined ceiling, the velocity profile of the main flow was compared along the P2 line. The distribution of the x-component velocity in Case 1 was compared between the calculational results of Method-DKQ, -EH, and -EK and the results are given in Fig. 33. Method-DKQ was based on the finite difference method, which approximated the inclined wall by the step-wise mesh configuration. Method-EK and -EH were based on the finite element method and the calculated inclined wall was a smooth boundary. In Method-DKQ, the velocity near the top wall was very small and the height of the maximum velocity point was 70 mm lower than the experimental results. The velocity distribution near the top wall in Method-EK showed good agreement with the measured distribution. These two methods both used the k-ε model. In Method-EH, the velocity near the inclined top wall was smaller than that of Method-EK, because the large viscosity (100 times larger than the molecular viscosity) of Method-EH led to overestimation of the thickness of the velocity boundary layer. The result suggested that, while the finite element method could be used to simulate the flow along inclined or rounded boundaries, the method requires an adequate turbulence model.

Characteristics of the flow near the inclined wall were compared among all the applied codes on the two points; the maximum value of v_x and the height of the maximum velocity point (Fig. 34). The comparisons shown in Fig. 35 revealed that the methods based on the finite element method (Method No. $\geq$ 11) gave more accurate estimations than those of the finite difference method. The step approximation in the finite

difference method was not adequate to simulate the velocity distribution of the flow along the inclined wall.

5.2 Penetration Flow

The penetration flow was predicted by seven of the nine applied methods for Case 1. Table 5 gives a summary of the comparisons of the predicted penetration depths. Here, the experimental data were the maximum depths at which the penetration flow was detected with a frequency of at least 1/1000 cps as described in the section 2.4.

For Case 1, all applied methods using the laminar flow model overestimated the maximum penetration depth. Among them, Method-DL1b, -DL1c, and -DL3S showed oscillatory behavior of the penetration depth. Figure 36 shows the history of the penetration depth predicted by Method-DL1b. The penetration depth varied with time and it became 0 cm as shown at 60 seconds. Such oscillatory behavior was observed in the experiment; the penetration depth changed from also 0 cm to a few cm (< 5 cm), however the time period of the oscillation was much shorter (a few seconds) than this calculation.

Method-DM1S, -EK, and Method-EH did not predict the penetration flow into the inlet channel. In these methods, turbulence models were incorporated. The first two methods used the turbulence models which were tuned for turbulent flows with higher Re numbers (> 10000).

Method-DM1, -DKQ, and Method-DAQ predicted the penetration flow. Penetration flow behaviors obtained from these methods were nearly stable in contrast to the experimental results. In Method-DM1, the mixing length model was used only in the channel region. Method-DKQ and -DAQ used the turbulence models which used the modified model constant C_1 (see Appendix-2). The temperature distribution calculated by Method-DKQ with $C_1 = 1.656$ is compared with that of an additional calculation with the standard constant $C_1 = 1.44$ for Case 1 in Fig. 37. The penetration flow was not predicted by the k-ε model with the standard constants. This is consistent with the result of Method-EK (see Table 5). This comparison shows that the constant C_1 had a large effect not only on the stratified flow but on the penetration flow.

The set of the calculations from Cases 1 to 4 could give the onset criteria of the penetration flow relative to the Re number; Gr number was nearly constant and Re number was varied as shown in Fig. 18. In the experiments, the onset condition of the penetration flow, $Gr/Re^2 = 0.55$, was between Case 3 and 4. Three methods, i.e., Method-DL1a, -DM1 and Method-DKQ, were applied to more than three Cases to narrow down the onset condition of the penetration flow. The predicted onset was between Case 2 and Case 3 by Method-DL1a, between Case 3 and 4 by Method-DM1, and between Case 2 and 3 by Method-DKQ. These results were considered to be in good agreement with the experimental results.

To predict the penetration flow, turbulence models played an important role. The calculations without any turbulence models overestimated the depth of penetration. The real penetration flow remained in the upper region because of the inertia of upward flow, loss of the negative buoyancy force due to the mixing with the upward hot flow, and shear stress between the penetration flow and the upward flow. The laminar model underestimated both shear stress and loss of the negative buoyancy force due to insufficient mixing. However, the calculations with the standard k-ε model could not predict the penetration. The calculation with k-ε model using the modified model constant, C_1 predicted the penetration flow well. Here, C_1 is the coefficient of the production term of the dissipation rate (see Appendix-2). Thus the increase of C_1

results in decrease of turbulent kinetic energy and turbulent viscosity. The modified k-ε model produced less turbulent mixing than the original k-ε model. These results strongly suggest that the amount of turbulence mixing is central to the prediction of penetration flow phenomena.

6. Summary and Conclusions

A benchmark exercise for thermohydraulic analysis codes was performed in the field of natural convection decay heat removals of liquid metal cooled fast breeder reactors. The benchmark problem focused on the thermal stratification and the penetration flow into a rectangular channel from a stratified cooled plenum, which simulated the plenum-core thermohydraulic interactions in a fast breeder reactor. The benchmark problem required participants to predict velocity and temperature fields in the cooled plenum, especially the stratified flow, which was root of the penetration flow. Further, the onset condition of the penetration flow and the penetration depth were required to predict among four cases of the upflow velocity in the inlet channel.

A total of 12 numerical methods were applied to the benchmark exercise by the participants from Germany, Italy, and Japan. The methods applied were ten of the finite difference methods and two of the finite element methods. An order of accuracy of the difference schemes for the convection terms varied from the first order up-wind to the third order skew up-wind. Besides the laminar flow model the following turbulence models were applied: mixing length model, k-ε models with standard constants and with the modified constant, and Algebraic Stress/flux Model.

From the benchmark exercise, the following conclusions were drawn.
(1) Plenum thermohydraulics
   - For higher order schemes of convection terms in the finite difference method, a turbulence model was required to avoid unphysical flow instability.
   - An advanced turbulence model was desired to simulate stratified flow, which had low Re number but still exhibited turbulent characteristics.
   - Forced flow along the inclined boundary was simulated better by the finite element method than the finite difference method without boundary fit schemes, when the finite element method was used with an adequate turbulence model.
(2) Penetration flow
   - The penetration flow was calculated by a few methods while the results showed a wide variation on the onset condition as well as the penetration depth.
   - The turbulent viscosity and turbulent mixing strongly influenced the penetration depth. Thus, improvement in turbulence models, especially for low Re and mixed convection flows, is important.

These analytical results of the benchmark problem suggested that the turbulence models, higher accurate schemes for convection terms and modeling of irregular boundaries are important in the computer code development to predict thermohydraulic phenomena in mixed convection flows and natural convection flows.

Implications obtained from the benchmark experiments render the following recommendations. From the water experiments, the onset condition of the penetration flow was shown to be $Gr/Re^2 > 0.55$ and the penetration depth was correlated with Gr/Re^2 and Re. Suppose typical design of fuel and blanket subassemblies with circular outlets 120 mm in diameter of a large scale liquid metal cooled fast breeder reactor. The averaged outlet velocity of the fuel and blanket assemblies were 10 cm/sec and 2 cm/sec, respectively, under natural circulation conditions (2 ~ 3% of the rated flow condition). Here, let the temperature differences between the outlet and the upper

plenum be 180 °C and 130 °C for the fuel subassembly and for the blanket subassembly, respectively. Then the values of Gr/Re^2 were 6 and 110 for the fuel subassembly and the blanket subassembly, respectively. These values were much larger than the critical value of 0.55. Therefore it seems certain that penetration flow would occur under actual operating conditions, especially for the blanket subassemblies, if the same critical value also applies to sodium systems. Consideration of the penetration phenomena is important to evaluate the safety of the decay heat removal by natural circulation using immersed coolers because the penetration flow influences the heat removal of the core. Sodium tests of the penetration flow into a channel are underway at O-arai Engineering Center of Power Reactor and Nuclear Fuel Development Corporation to better understand the penetration phenomena in sodium system[9].

Acknowledgment

Nomenclature

A_c surface area of the cold wall (m^2),

A_{in} cross section area of the inlet channel (m^2),

D hydraulic equivalent diameter of the inlet channel (m),

q'' heat flux through the cold wall used for the boundary condition (W/m^2),

Q total heat removed by cooling box (W),

T_{av} averaged temperature of the channel inlet temperature and the temperature at the bottom of the P1 line in the plenum (°C),

v_{av} average velocity on the x-z plane (y = 0 mm) at the inlet channel (m/sec),

v_z averaged velocity at the channel inlet (m/sec),

W volumetric flow rate in the inlet channel (m^3/sec.),

β thermal expansion rate of water at T_{av} (1/°C),

ΔT the difference between the channel inlet temperature and the temperature at the bottom of the P1 line in the plenum (°C), and

ν kinetic viscosity of water at T_{av} (m^2/sec).

References

[1]   Report on the 7th Meeting of the IAHR Working Group on Advanced Nuclear Reactors Thermal Hydraulics, IAHR Bulletin Vol. 8-1991 p.72.

[2]   Satoh, K and Miyakoshi, H., Study of Decay Heat Removal by Natural Circulation - Transition from Forced to Natural Circulation Flow -, Proc. 4th Inter. Topical Meeting on Nuclear Reactor Thermal-Hydraulics, Volume 1, p. 378, Karlsruhe, F.R. Germany, Oct. 1989.

[3]   Ieda, Y. and Hayashi, K. et al., Thermohydraulic Study on Natural Circulation Decay Heat Removal for a Pool-type LMFBR, Proc. Inter. Conf. on Fast Reactors and Related Fuel Cycles, Volume II, p. 16.9-1, Kyoto, Japan, Oct. 1991.

[4]   Jerng, D.W. and Todreas, N.E., Mixed Convective Flow Penetration in Vertical Channels, Proc. 5th Inter. Meeting on Reactor Thermal Hydraulics, p.1720, Salt Lake City, USA, Sep. 1992.

[5]   Modi, V. and Torrance. K.E., Experimental and Numerical Studies of Cold Inflow at the Exit of Buoyant Channel Flows, Journal of Heat Transfer, Volume 109, pp.392-399, (1987).

[6]   Barakat, A.I. and Todreas, N.E., Mixed Convection Buoyancy-Induced Backflow in a Vertical Single Rod Channel Connected to an Upper Plenum, Proc. 4th Inter. Topical Meeting on Nuclear Reactor Thermal-Hydraulics Volume 2, p. 746, Karlsruhe, F.R. Germany, Oct. 1989.

[7]   Rodi W., Turbulence Models for Environmental Problems, Prediction Methods for Turbulent Flows, Hemisphere Publishing Corporation, (1980).

[8]   Launder, B.E. and Spalding, D.B., The numerical Computation of Turbulence Flows, Comp. Methods Apple. Mech. Eng., Vol. 3 p. 269, (1974).

[9]   Toda, S. and Ieda, Y., et al., Transverse Temperature Distribution in a Multi-subassembly Test Section simulating Natural Circulation Decay Heat Removal in the LMFBR, Proc. Inter. Conf. on Design and Safety of Advanced Nuclear Power Plants, Volume III, p. 26.1-1, Tokyo, Japan, Oct. 1992.

[10]   Fraikin, M.P. and Portier, J.J., et al., Application of a k-ε turbulence model to an enclosed buoyancy driven recirculating flow, Chem. Eng. Commun. Vol. 13, pp.289-314, (1982).

Table 1 Experimental Parameters of Benchmark Problems

	Case 1	Case 2	Case3	Case 4
Inlet temperature of the test section	48.9 °C	49.0	49.1	49.1
Flow rate into the test section	18.0 l/min	22.5	27.0	45.0
Inlet temperature of the cooling box	12.6 °C	11.9	12.1	13.1
Flow rate into the cooling box		25.0 l/min		

Table 2 Boundary Conditions of Benchmark Problem

Conditions	Case 1	Case 2	Case 3	Case 4
Inlet Temperature (°C)	48.9	49.0	49.1	49.1
Average Inlet Velocity (cm/s)	4.15	5.16	6.34	11.4
Outlet Boundary Pressure (Pa)	Constant ($P=1.0132\times10^5$)			
Cold Wall Temperature (°C)	14.8	14.4	14.5	15.4
Heat Flux (W/m^2) on the Cold Wall	-2.13×10^4	-2.24×10^4	-2.34×10^4	-2.40×10^4
Bottom Wall Temperature (°C)*	37.0	36.7	36.4	38.5

* Temperature at the bottom of the traverse line P4

Table 3 Applied Analysis Methods

No.	Method	Numerical scheme	Turbulence model	Convection term	Cold wall option*	Applied cases	Mesh number (total)
1	DL1a	FDM	Laminar	1st order up-wind scheme	1	1,2,3,4	(4950)
2	DL1b	FDM	Laminar	1st order up-wind	1	1	89 x 99
3	DL1c	FDM	Laminar	1st order up-wind	1	1,4	(5181) 76 x 122
4	DL1d	FDM	Laminar	1st order up-wind	1	4	72 x 99
5	DL3	FDM	Laminar	3rd order up-wind	1	4	(3892) 86 x 112
6	DL3S	FDM	Laminar	3rd order skew up-wind	1	1,4	45 x 117
7	DM1	FDM	Mixing length model	1st order up-wind	1	1, 3, 4	81 x 99
8	DM1S	FDM	Mixing length model	1st order skew up-wind	1	1, 4	54 x 76
9	DKQ	FDM	k-ε model (C_1:+15%)	QUICK+FRAM	2	1, 2, 3, 4	67 x 63
10	DAQ	FDM	ASM (C_1:+15%)	QUICK+FRAM	2	1,4	(2468) 67 x 63
11	EH	FEM	Homogeneous turbulent viscosity	9 node quadratic isoparameter element	2	1,4	(2468) 55 x 87 (2845 nodes)
12	EK	FEM	k-ε model	4 node quadrilateral element	2	1,4	(4413 nodes)

* Cold wall option; 1/ Constant temperature condition, 2/ Constant heat flux condition
Note; Method-DL1d, -DKQ and -DAQ are variations of one computer code.

Table 4　Prediction of Maximum Penetration Depth

		Case 1	Case 2	Case 3	Case 4
Measured Depth		5 cm	3 cm	1 cm	No*
No.	Method	Calculated Depth			
1	DL1a	16.6 cm	3.5	No	No
2	DL1b	25.**	—	—	—
3	DL1c	4.**	—	—	No
4	DL1d	—	—	—	No
5	DL3	—	—	—	>20.
6	DL3S	6.8**	—	—	No
7	DM1	>10.	—	0.8	No
8	DM1S	No	—	—	No
9	DKQ	8.5	1.2	No	No
10	DAQ	7.8	—	—	No
11	EK	No	—	—	No
12	EH	No	—	—	No

* No : No penetration was observed.

** Oscillation of the penetration depth was observed.
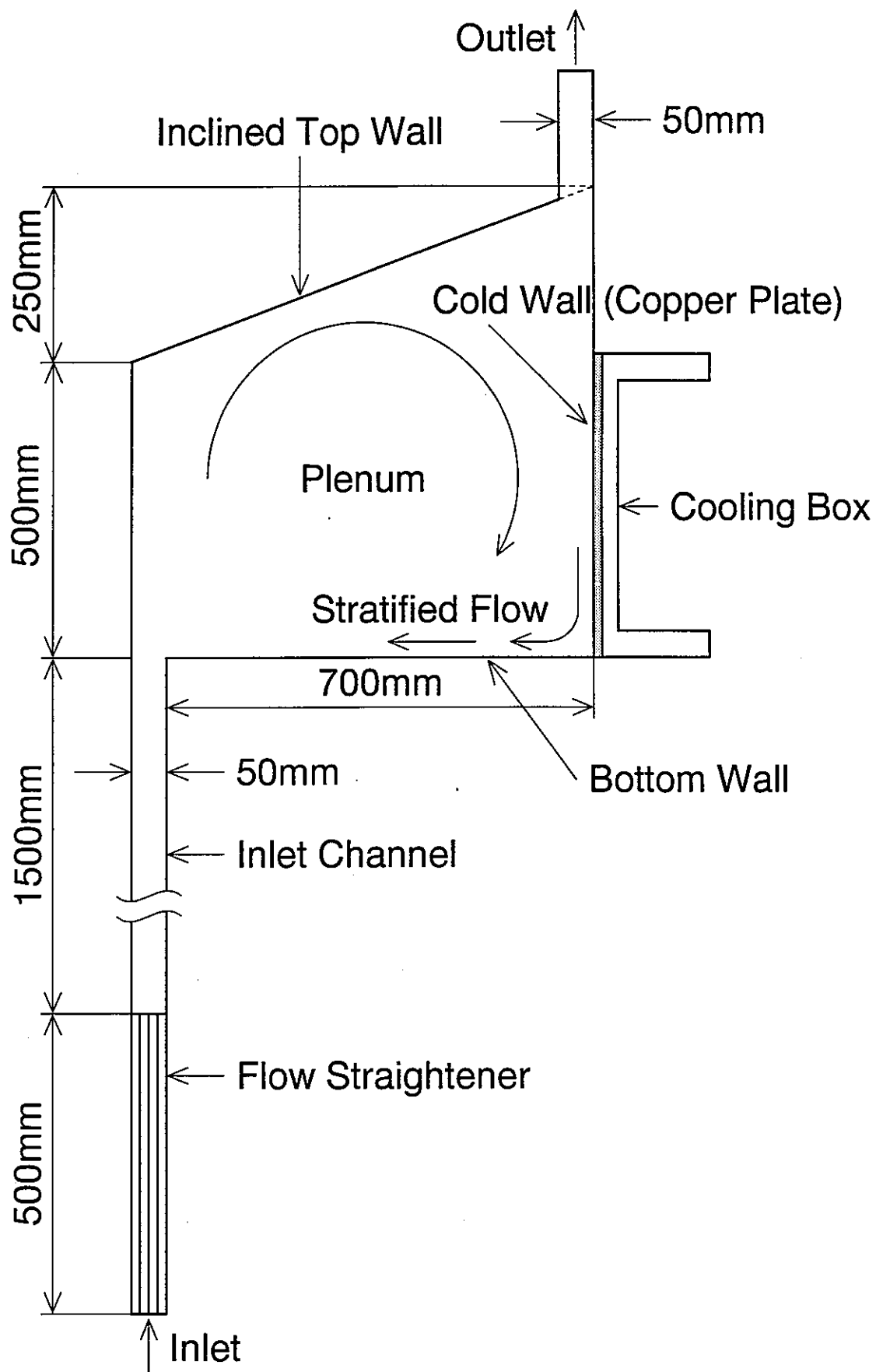
Fig.1 Schematic of Test Section
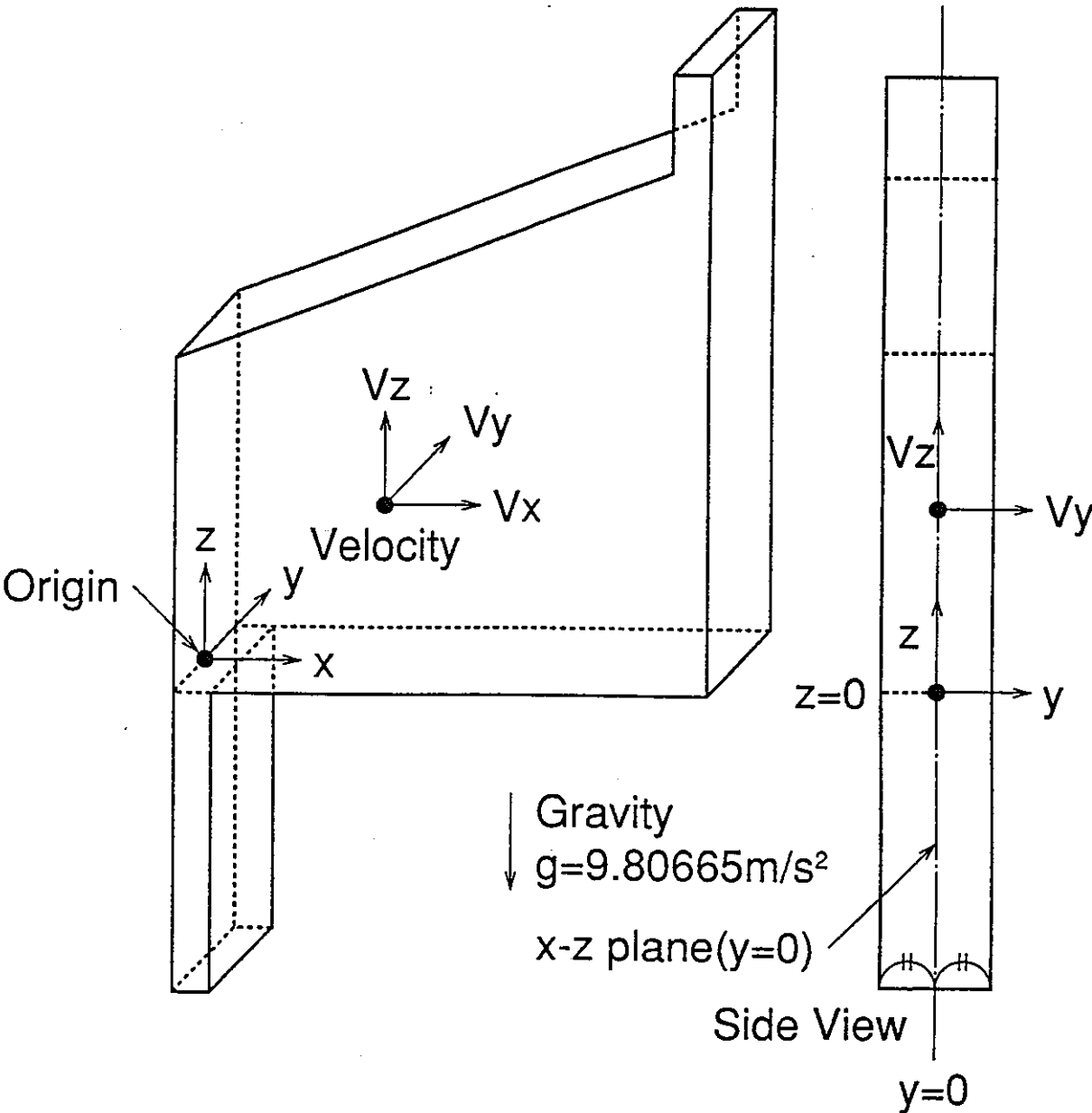
Fig. 2　Coordinate System
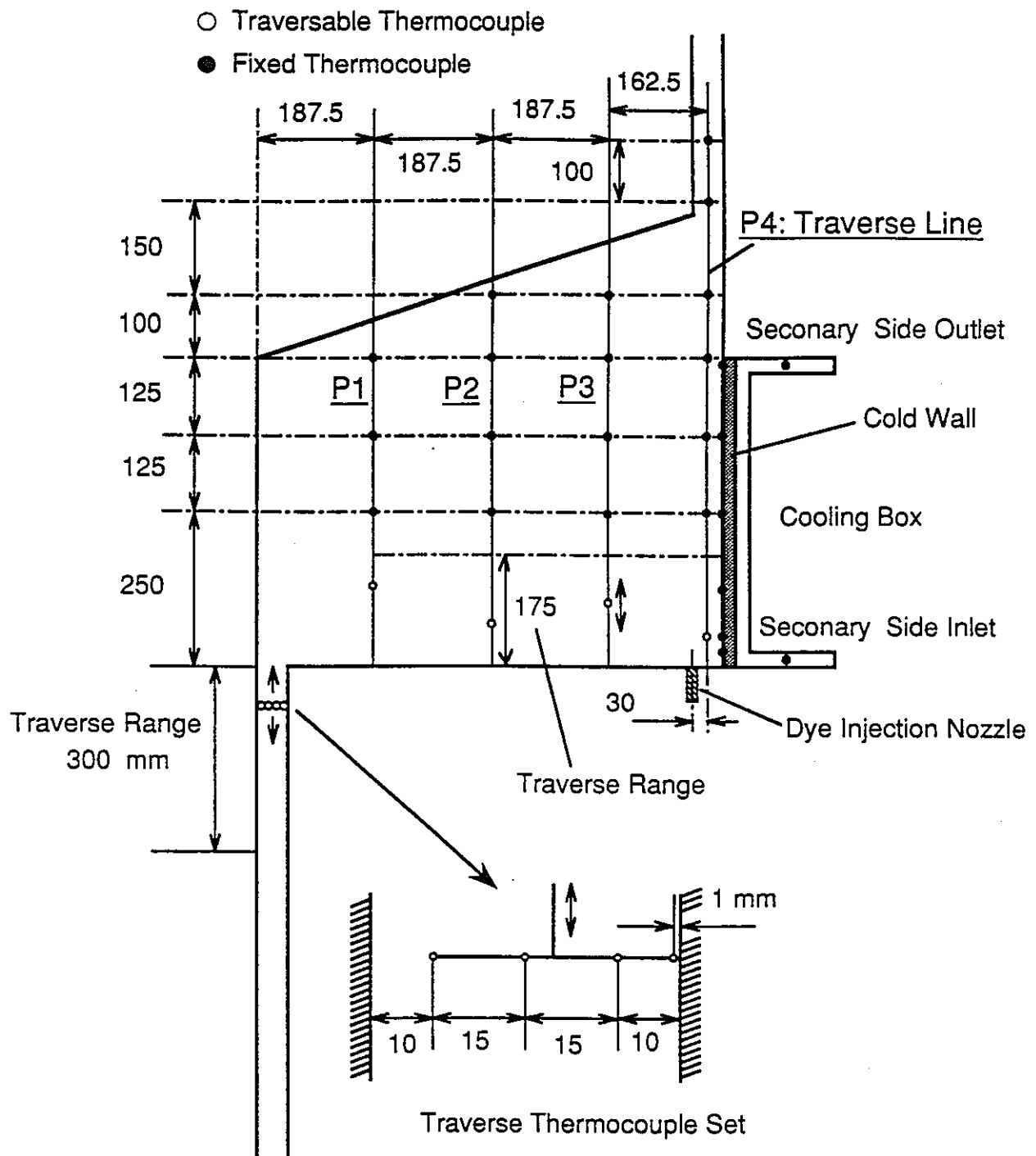
Fig. 3   Thermocouple Configuration

10 cm/sec

→

A

Case 1

Case 4
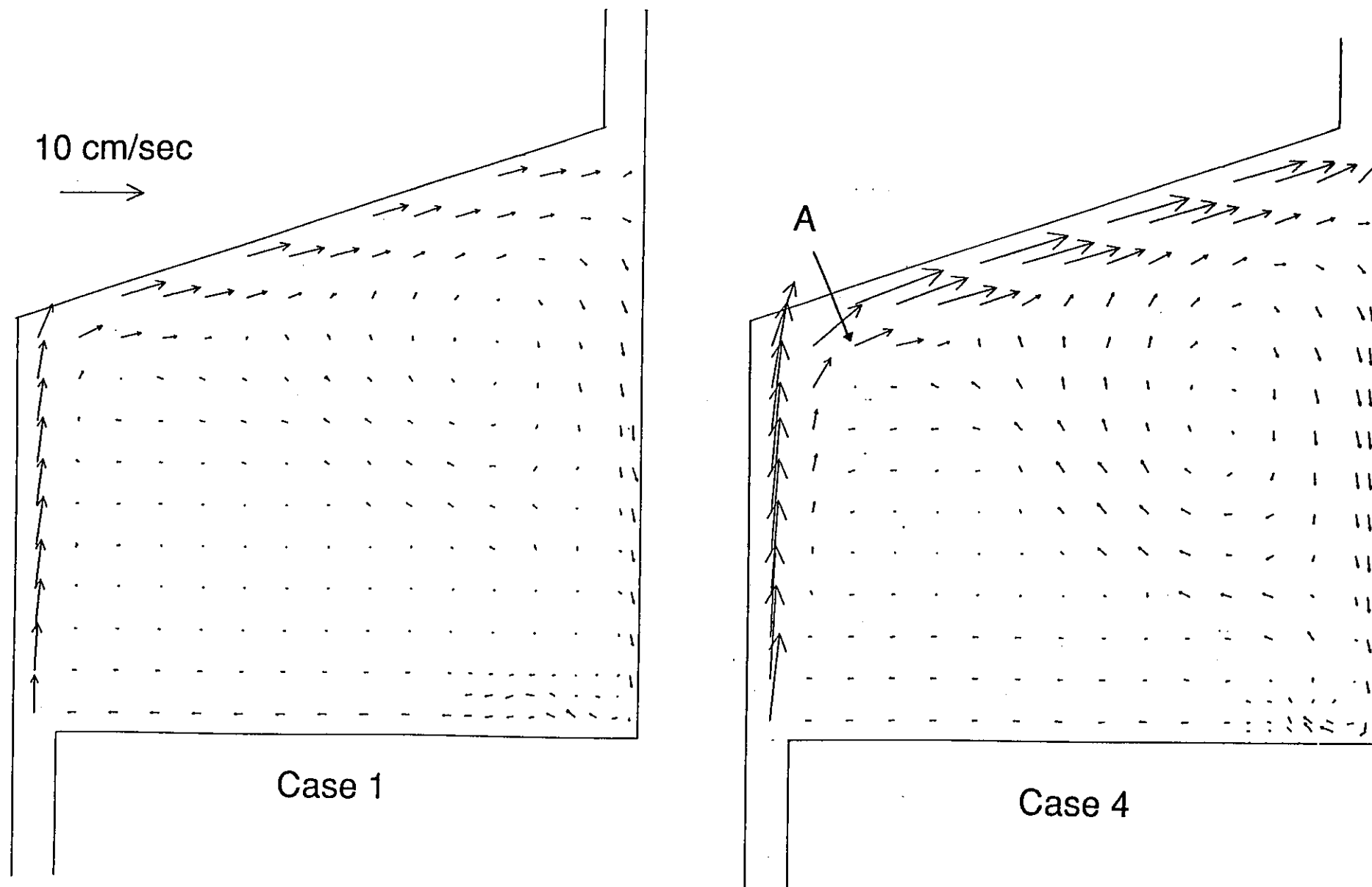
Fig. 4　Velocity Vector Fields in the Plenum in Cases 1 and 4
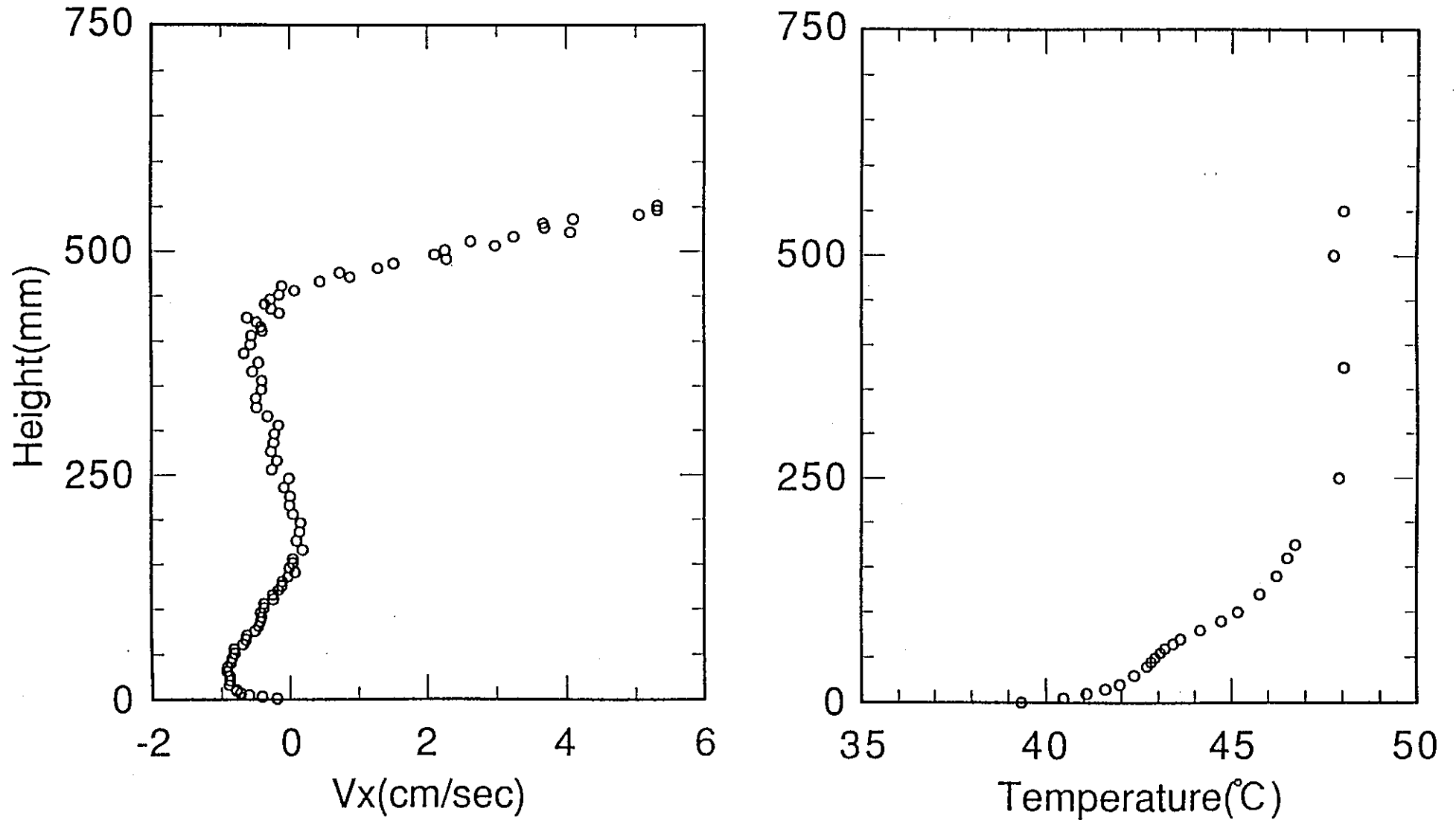
Fig. 5   Velocity and Temperature Distributions along P1 Line in Case 1
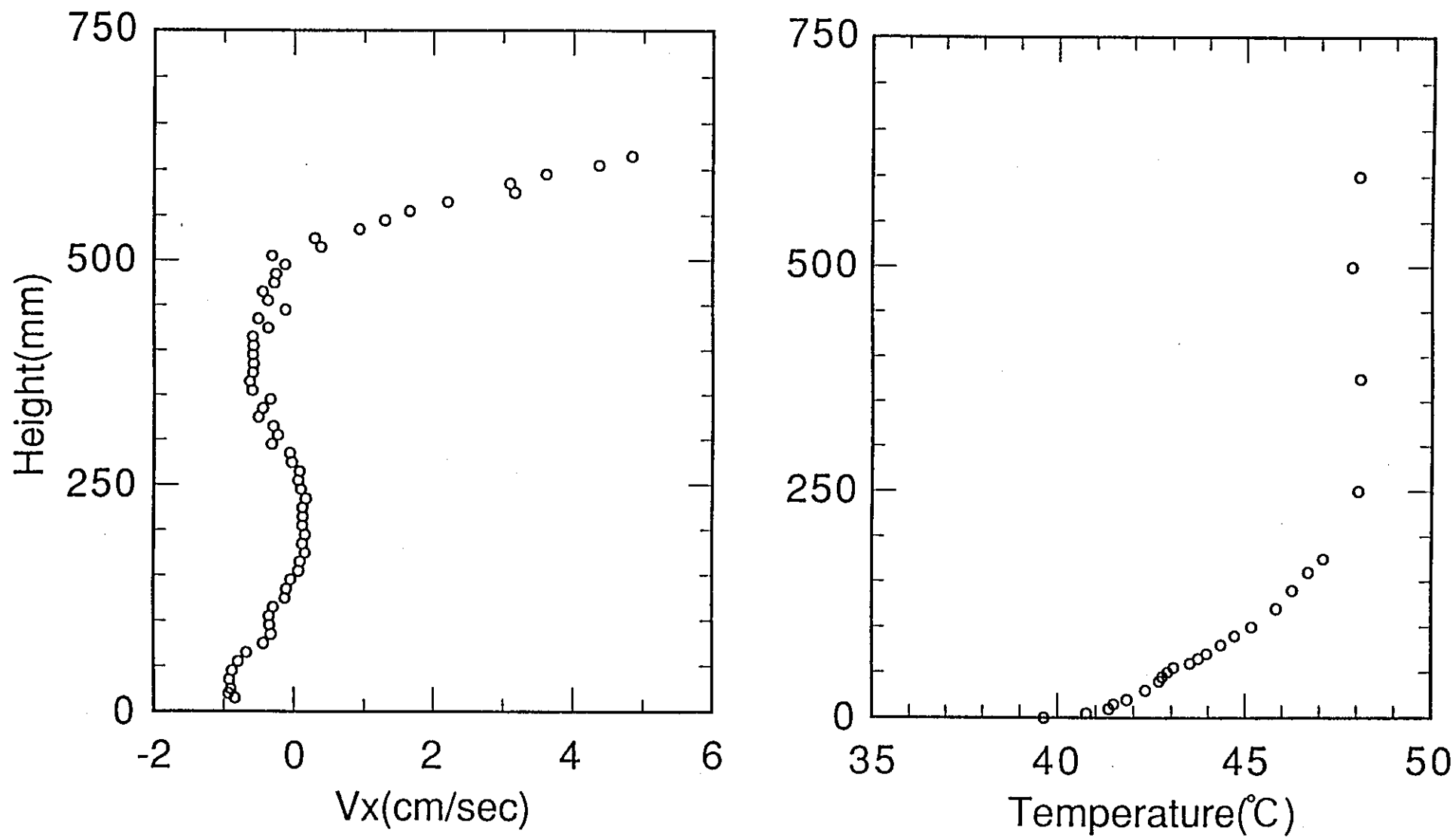
Fig. 6   Velocity and Temperature Distributions along P2 Line in Case 1
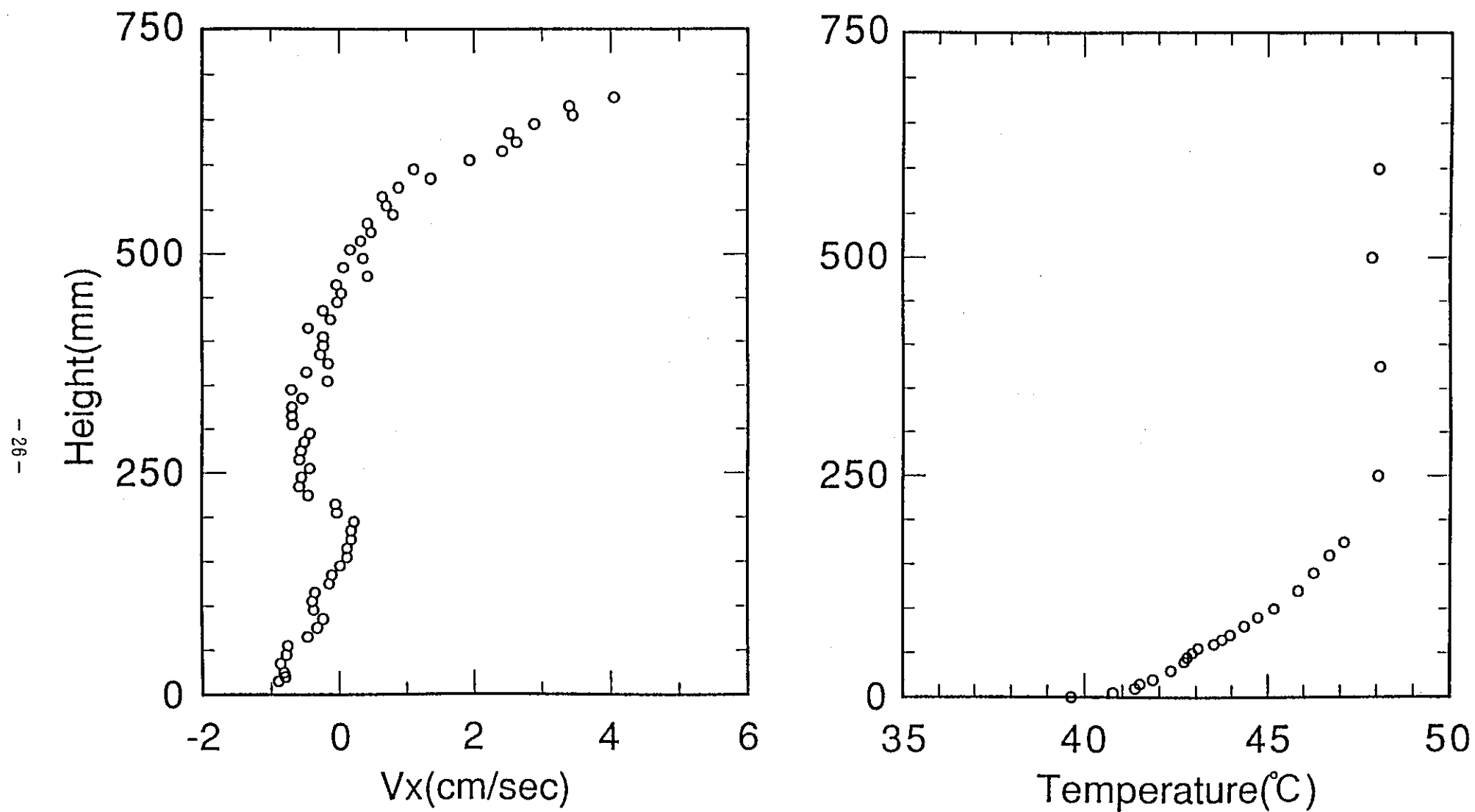
Fig. 7   Velocity and Temperature Distributions along P3 Line in Case 1
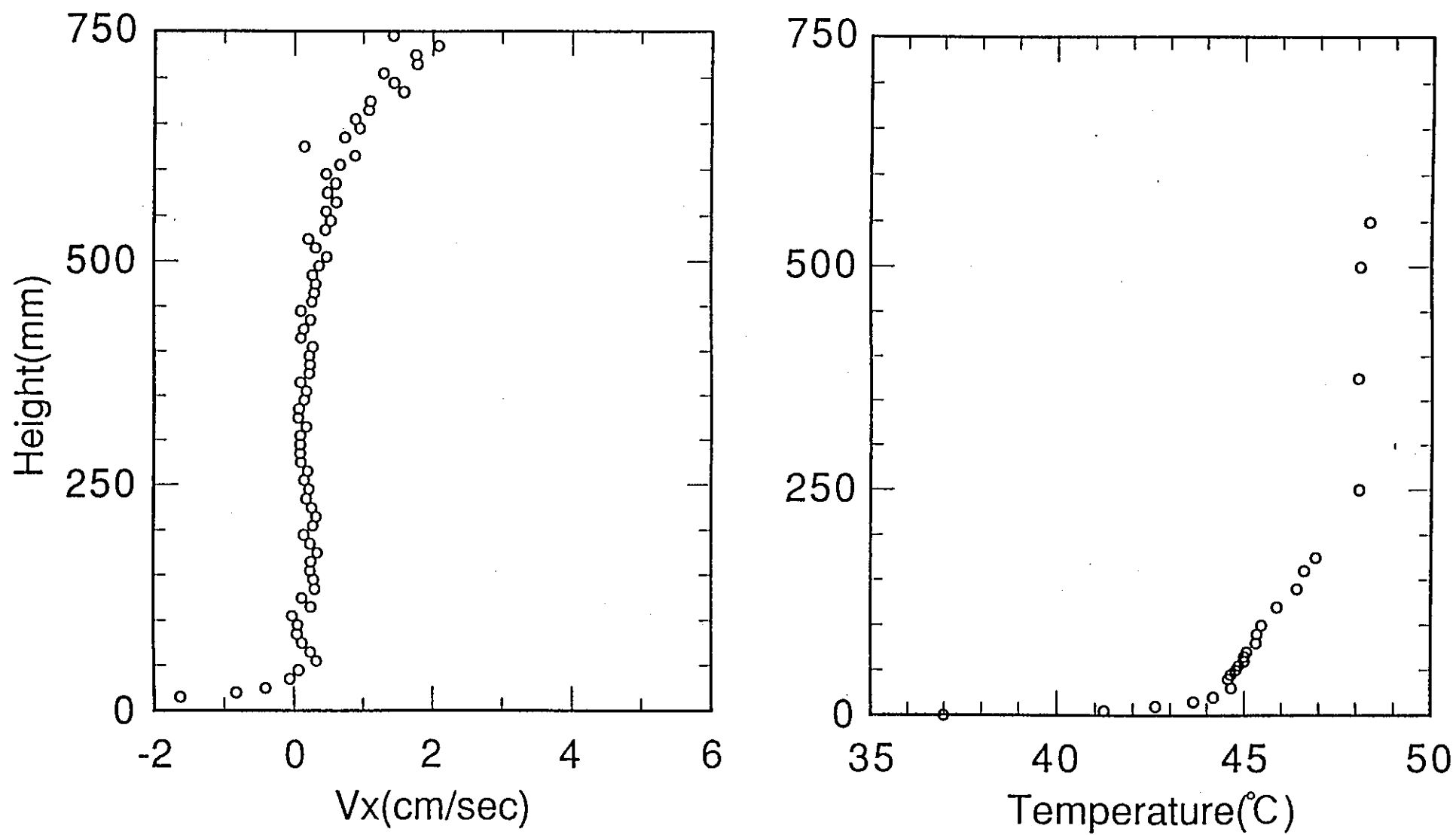
Fig. 8　Velocity and Temperature Distributions along P4 Line in Case 1
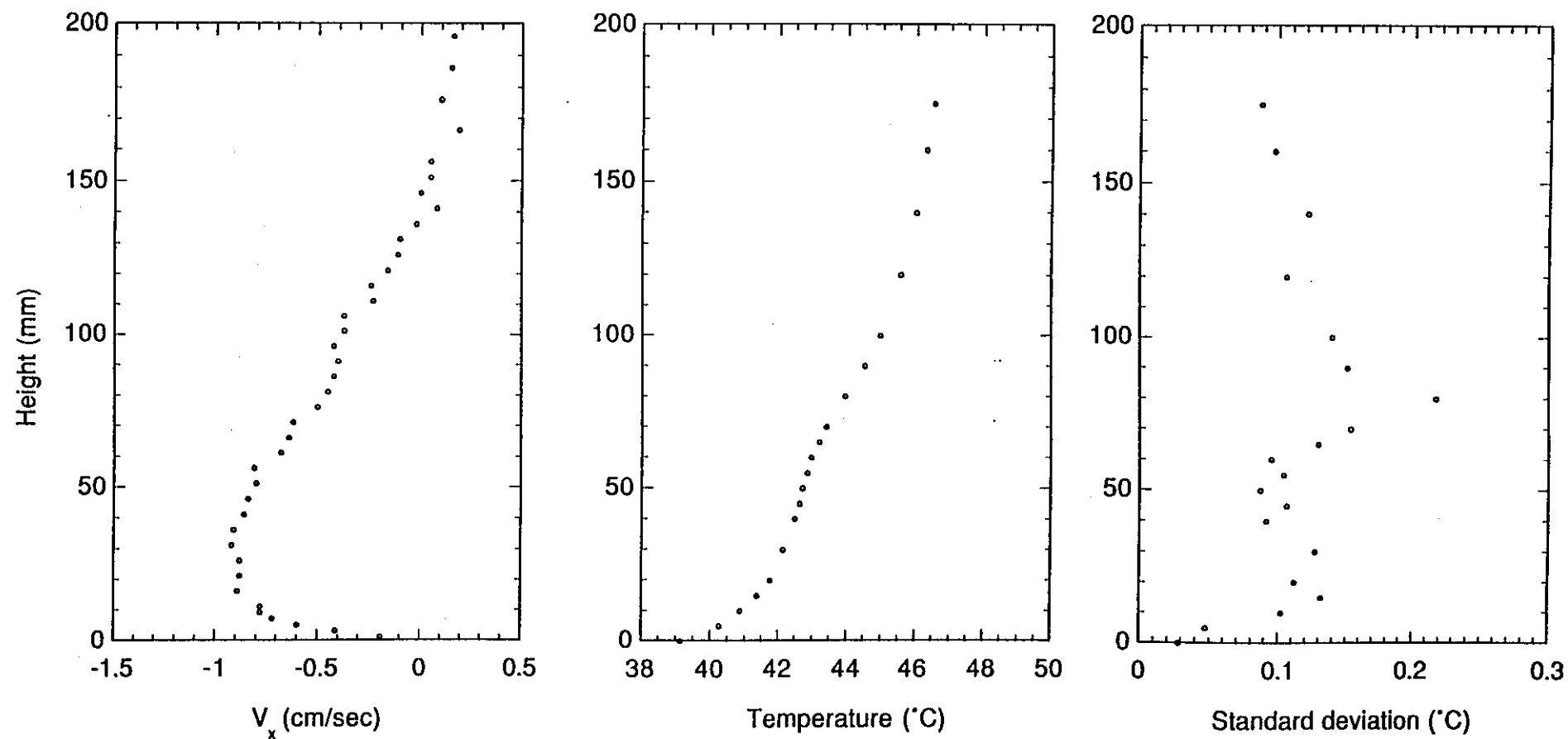
Fig. 9   Standard Deviation of Temperature across the Stratified Flow
          along P1 Line in Case 1
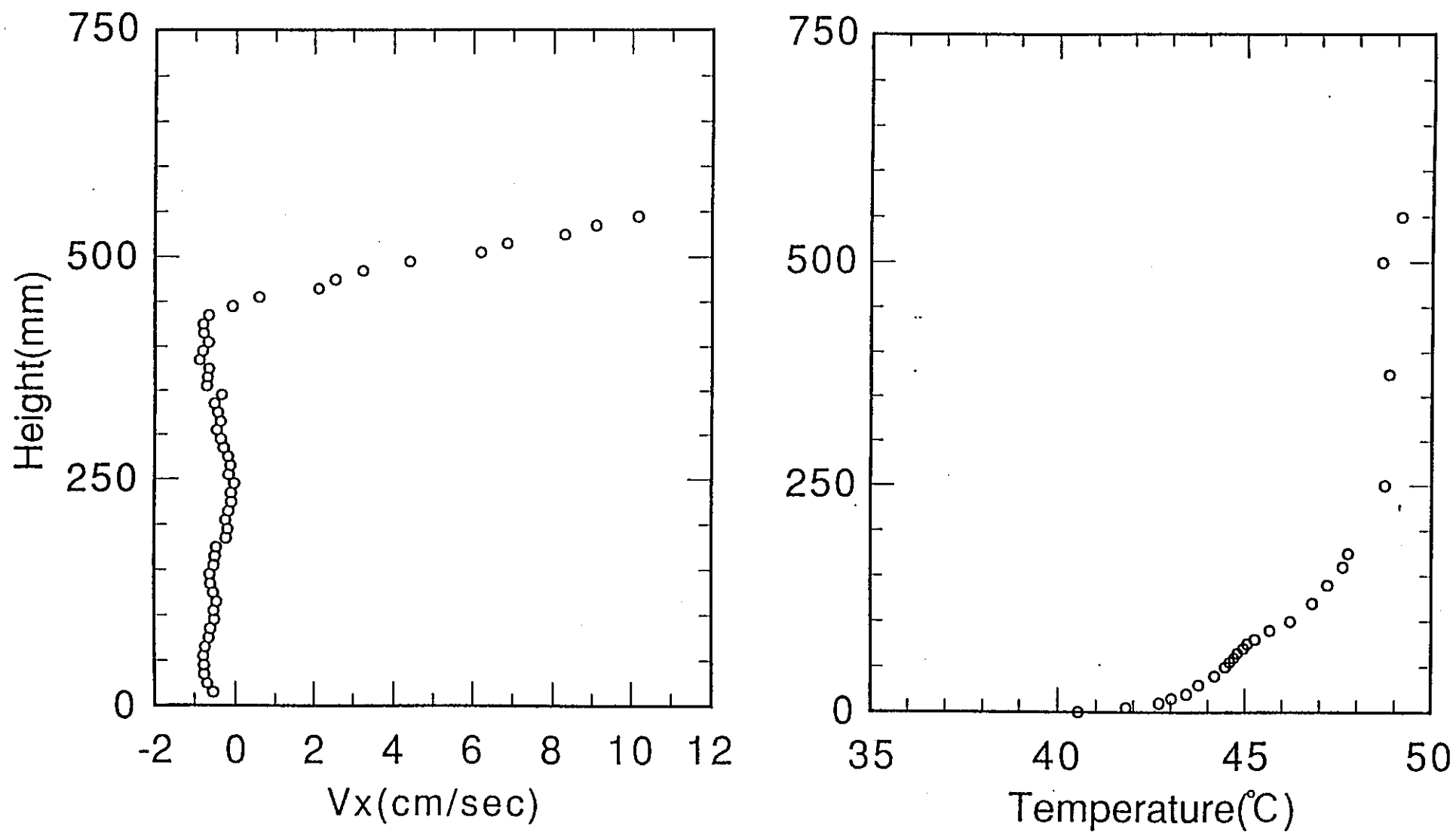
Fig. 10   Velocity and Temperature Distributions along P1 Line in Case 4
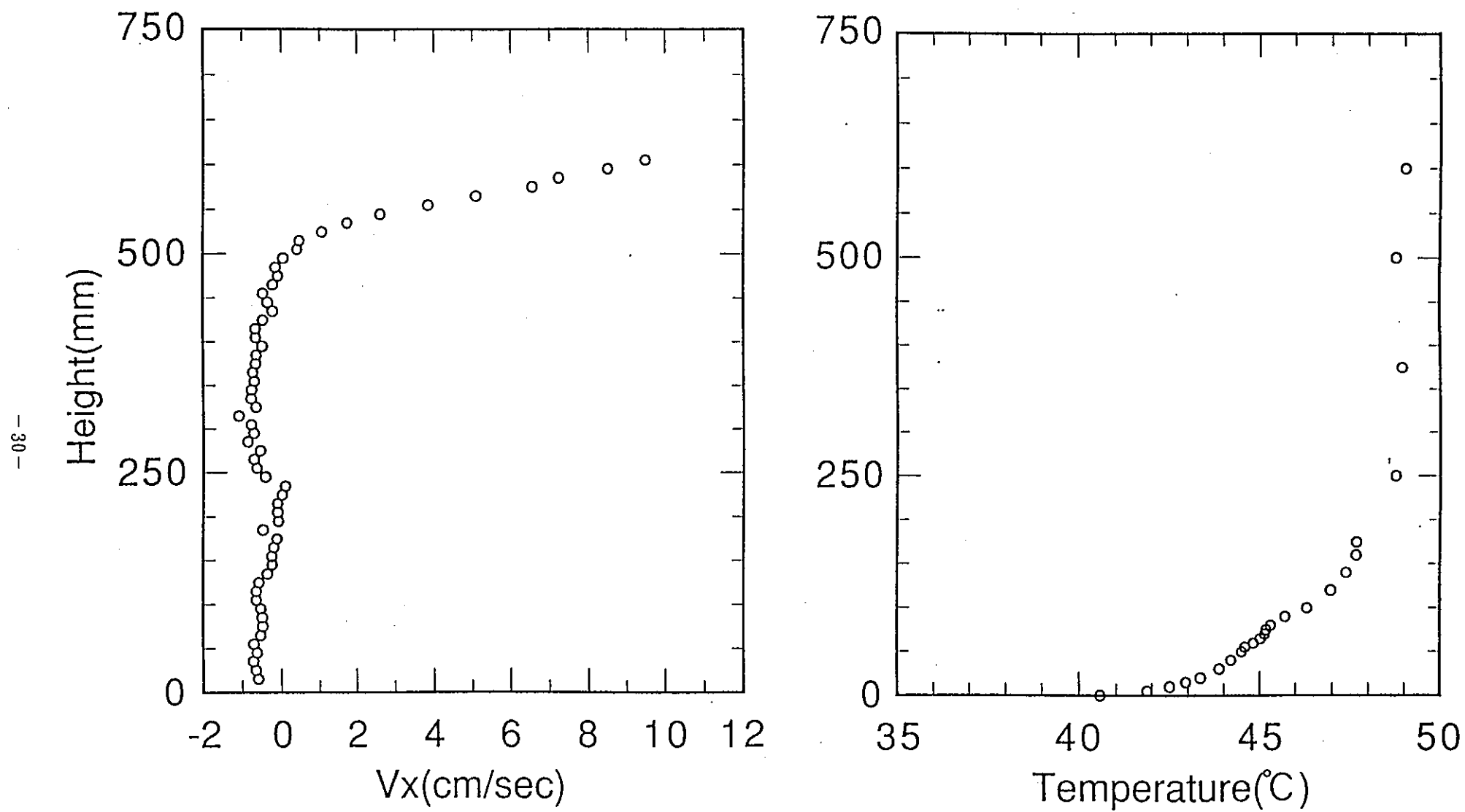
Fig. 11   Velocity and Temperature Distributions along P2 Line in Case 4
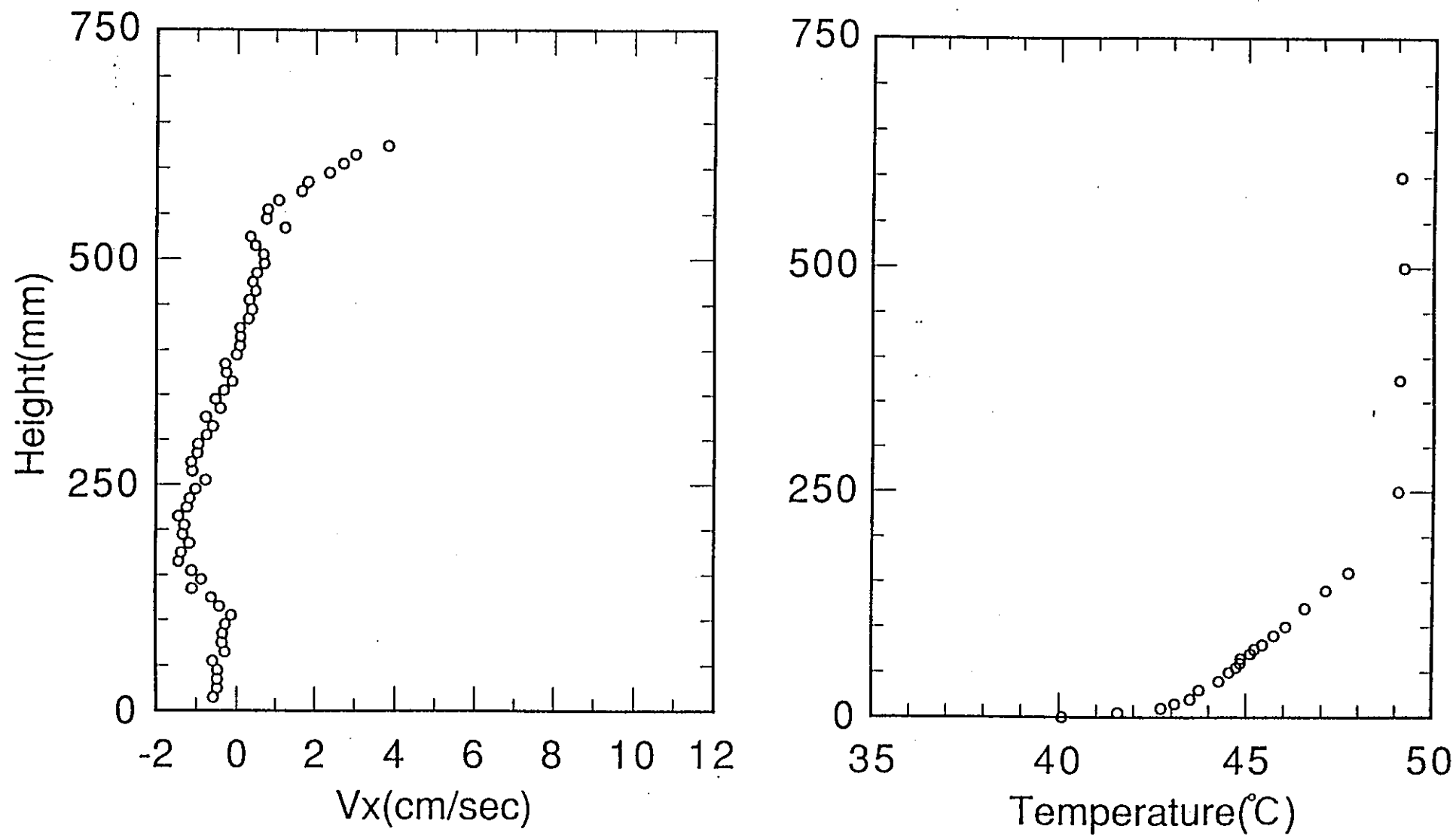
Fig. 12   Velocity and Temperature Distributions along P3 Line in Case 4
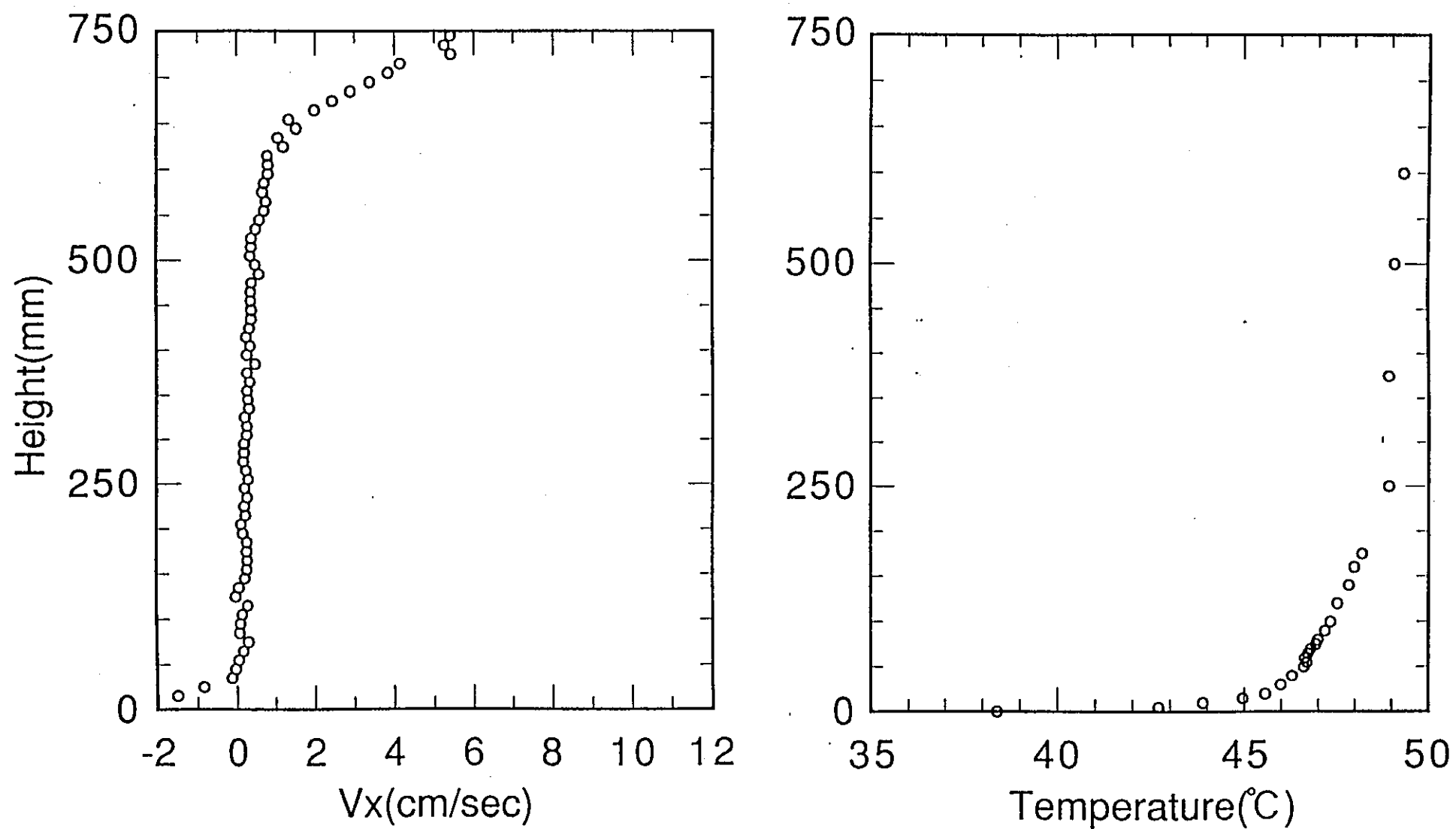
Fig. 13　Velocity and Temperature Distributions along P4 Line in Case 4
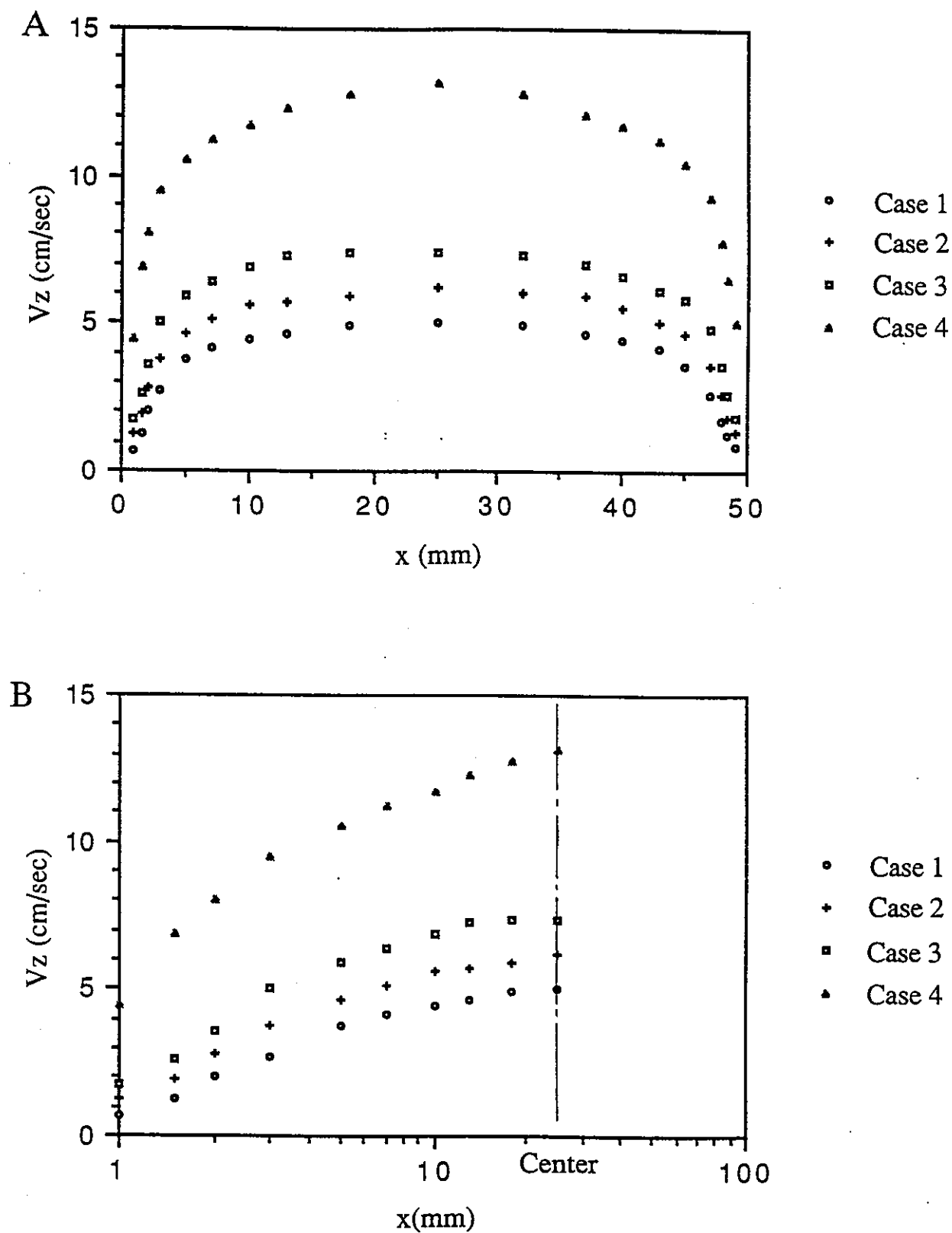
Fig. 14   Profile of Velocity Component (v_z) in x-direction at z= -200 mm
in the Inlet Channel
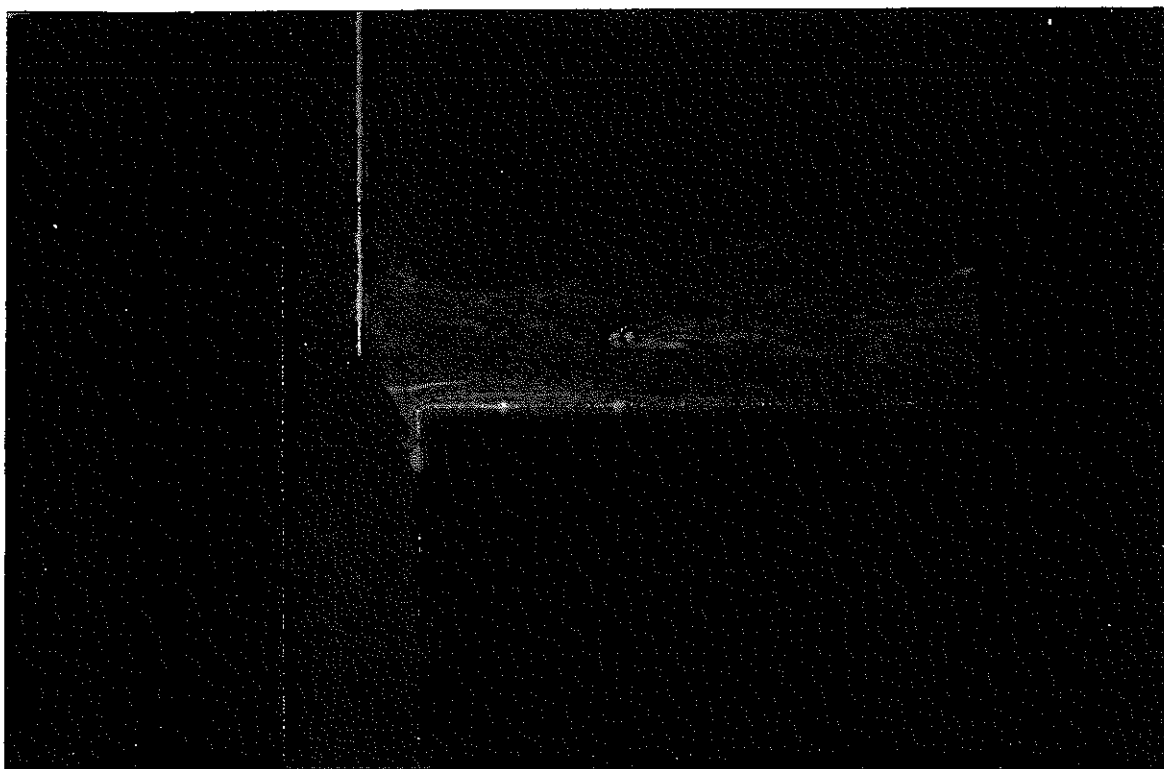
Fig. 15   Visualization of Penetration Flow into the Inlet Channel
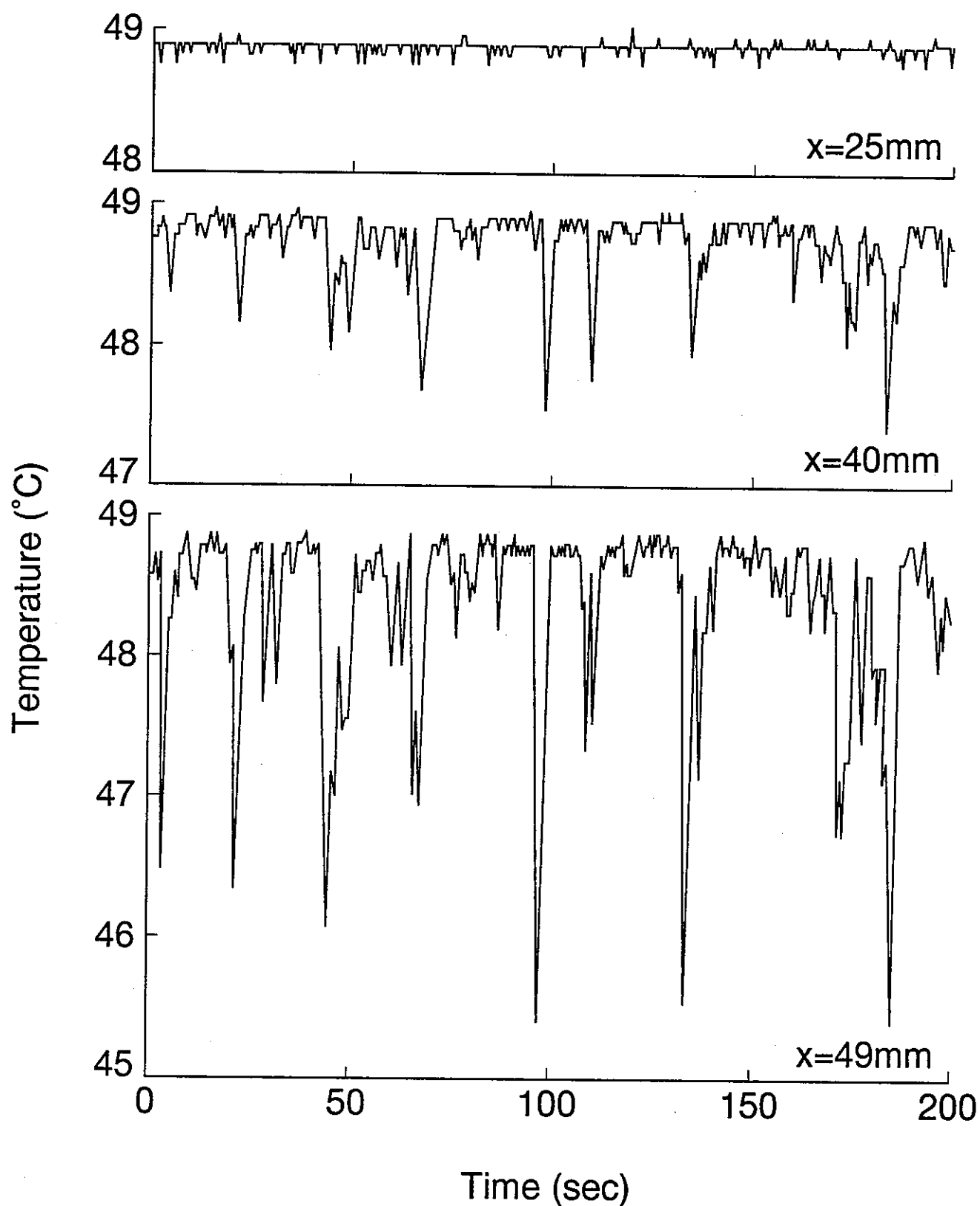
Fig. 16 Temperature Fluctuations at z=-10mm in the Inlet
Channel in Case 1
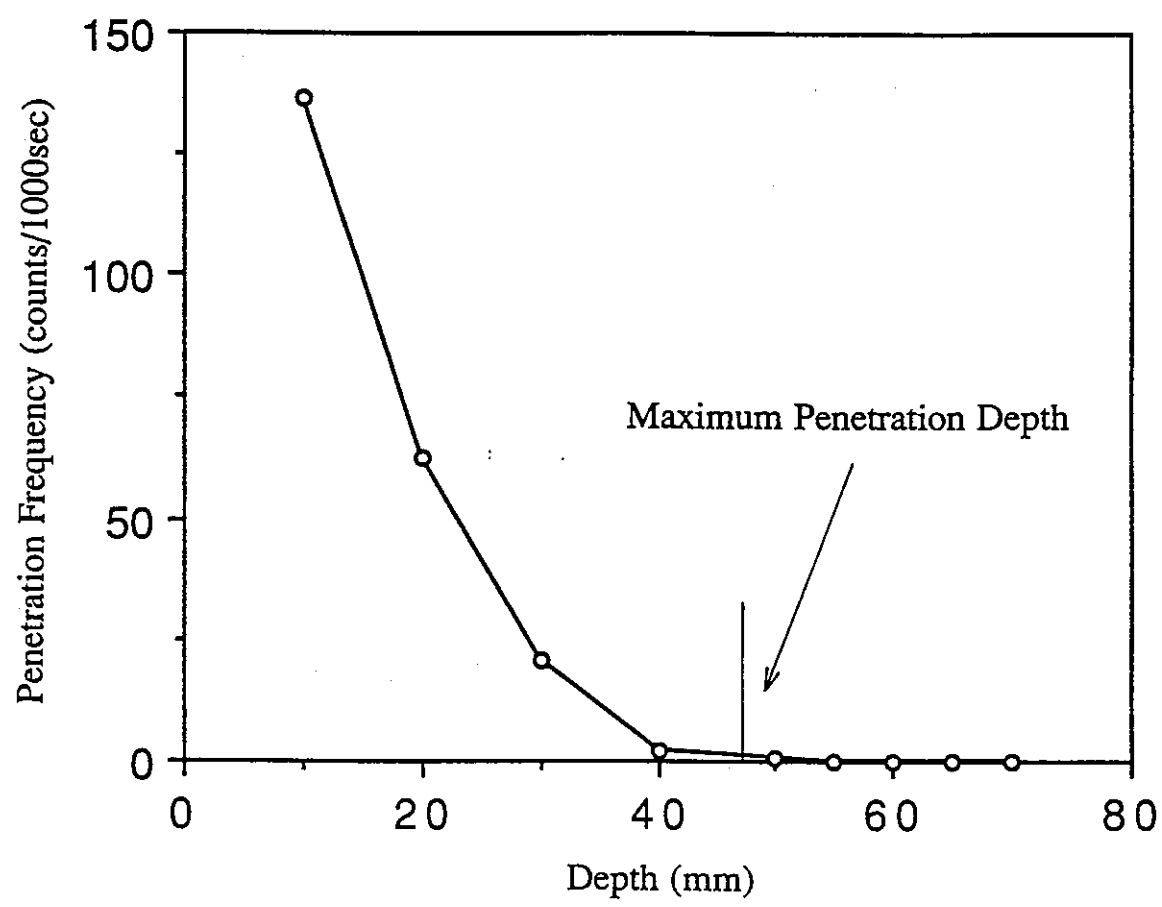
Fig. 17   Frequency of Penetration Flow in Case 1
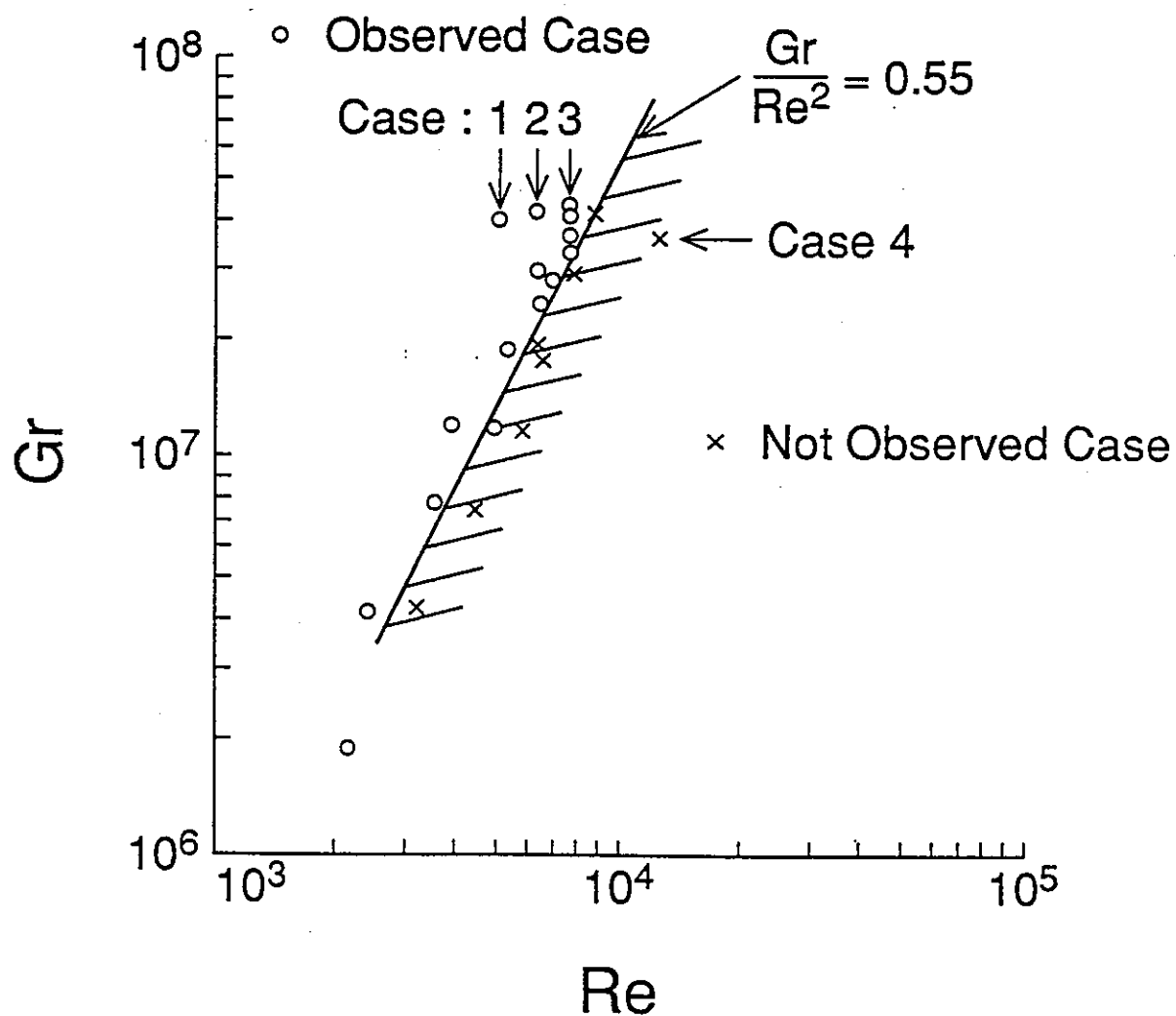
Fig.18 Occurrence Map of Penetration Flow
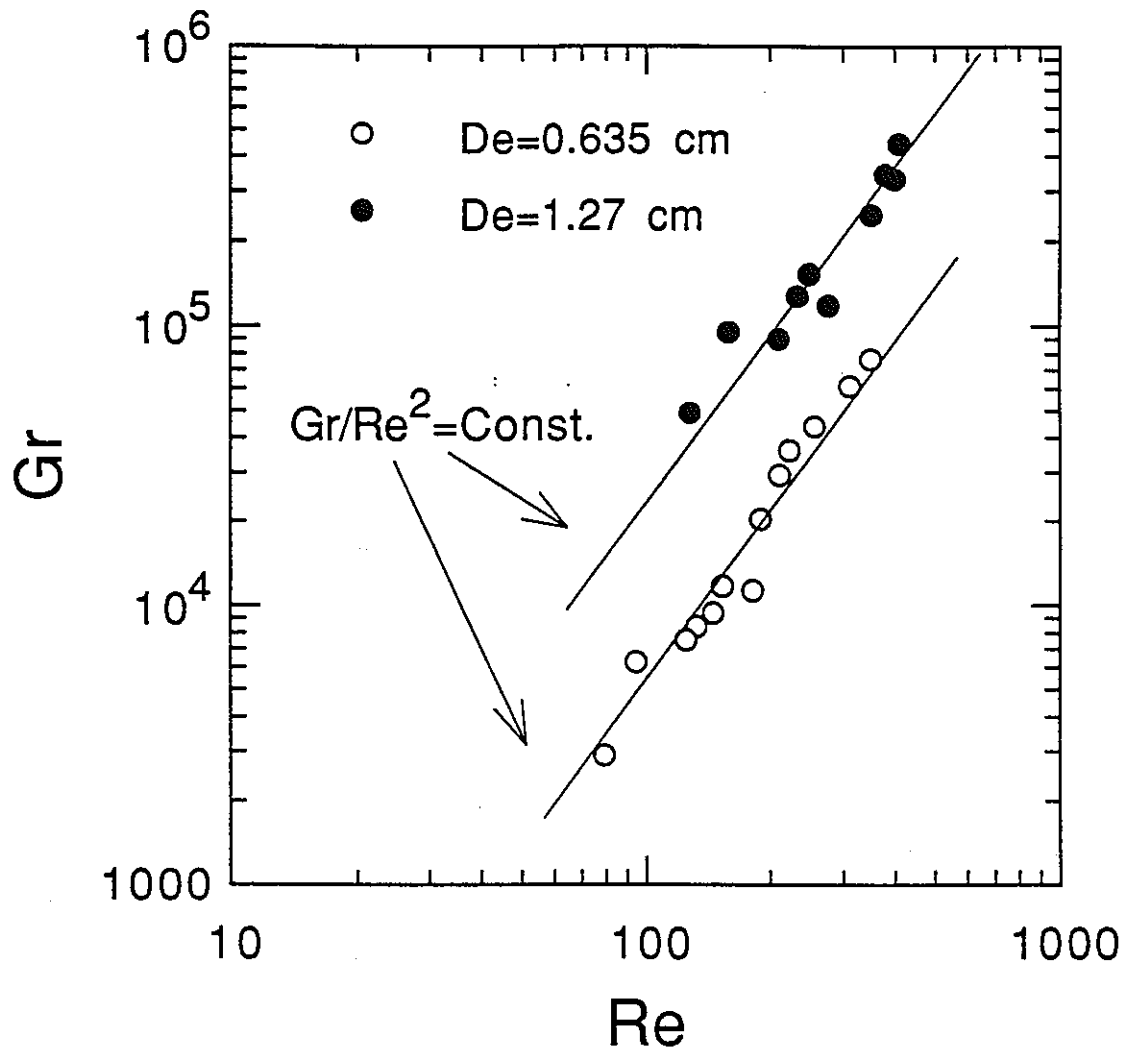
Fig. 19　Onset Conditions of Penetration Flow obtained by Barakat
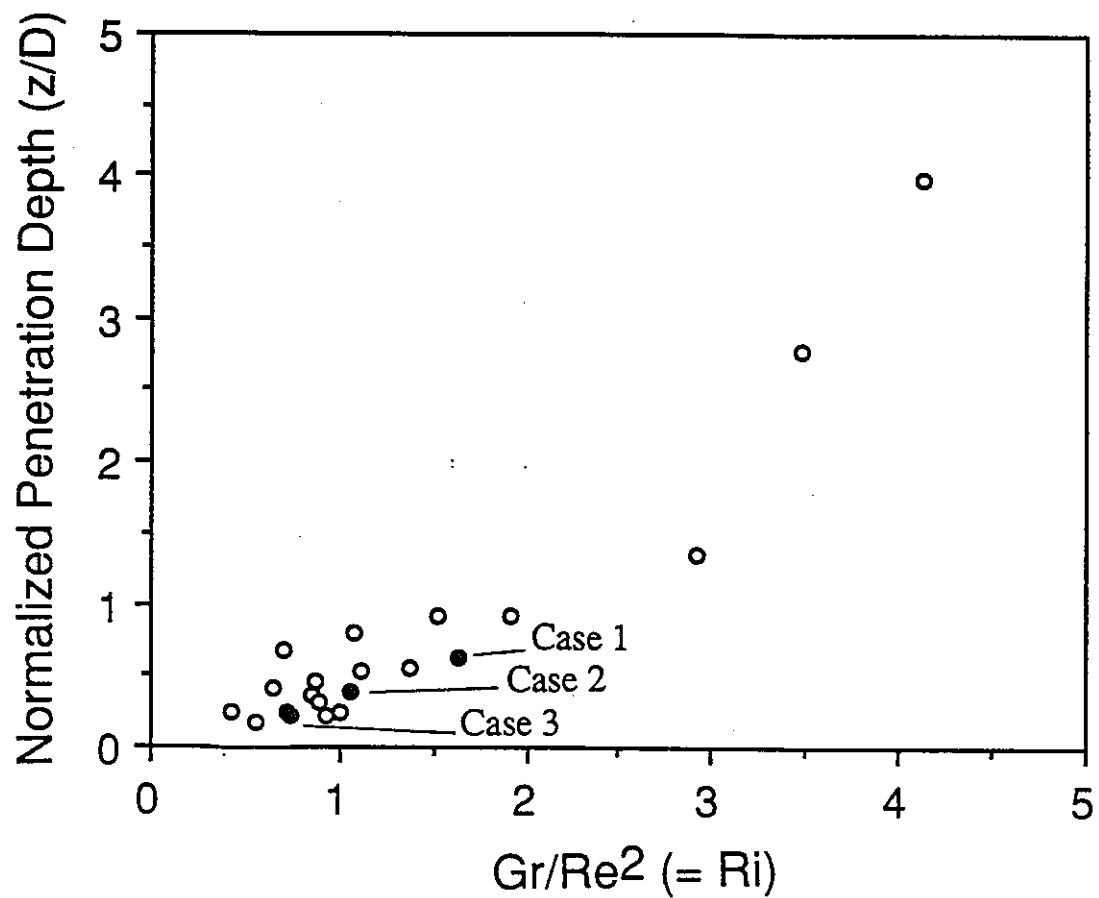
Fig. 20   Maximum Penetration Depth with respect to Ri Number

(x 10⁻⁴)

Normalized Penetration
Depth (z/D)
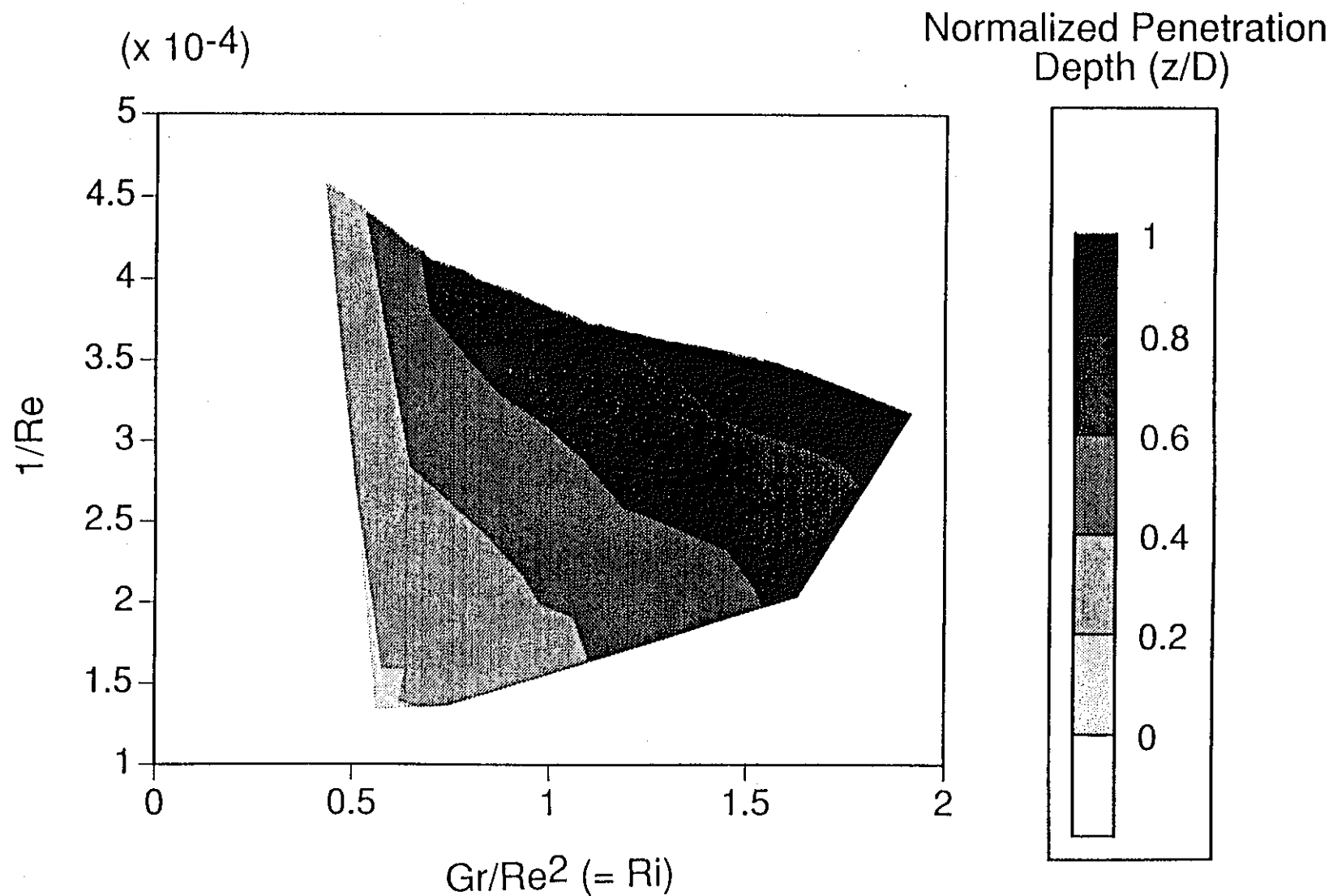
Fig. 21 Maximum Penetration Depth with respect to Ri and 1/Re
Numbers

10 cm/sec
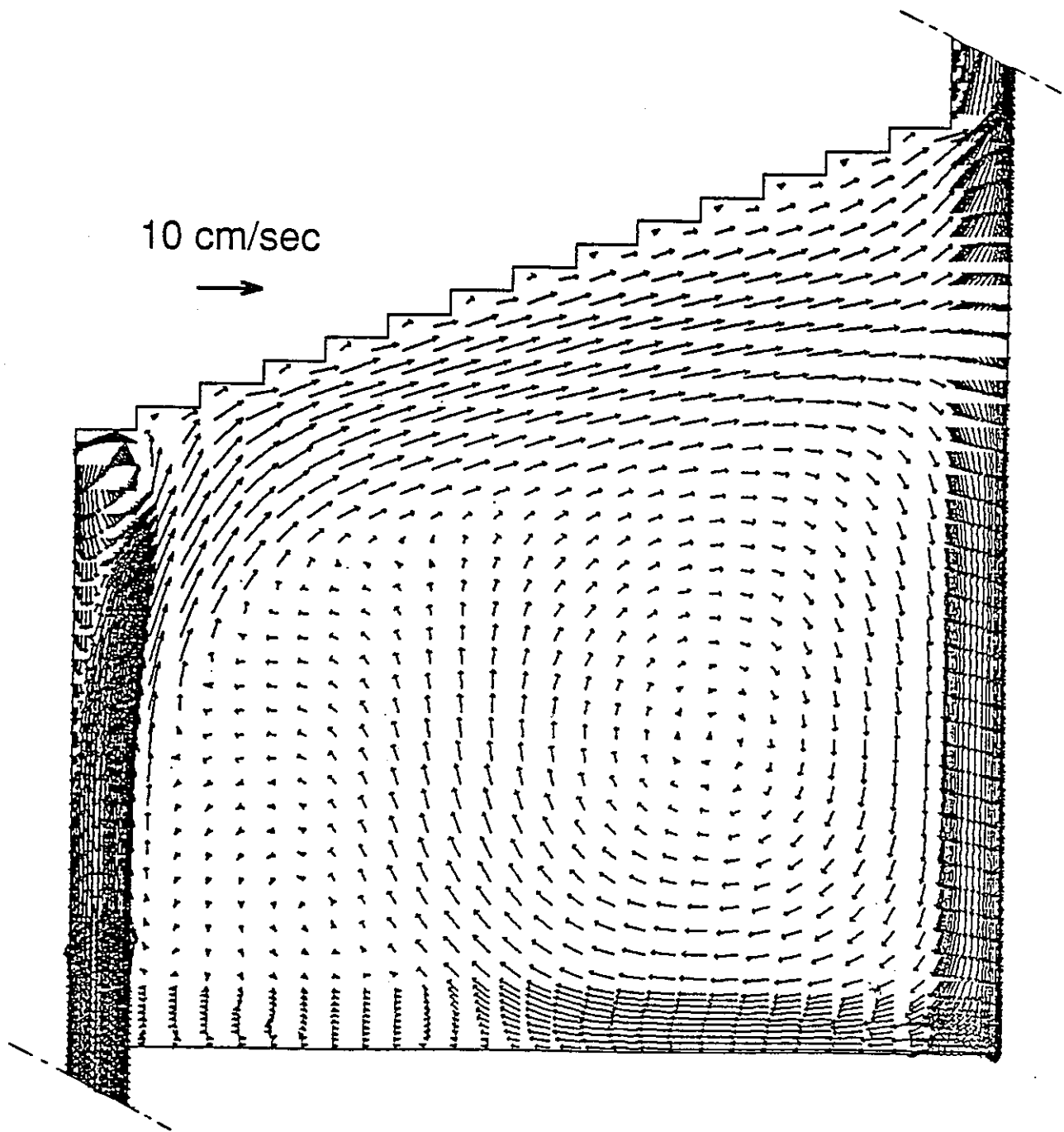
Fig. 22(a) Calculated Velocity Vector Field in Case 4 by Method-DL1a

10 cm/sec

→
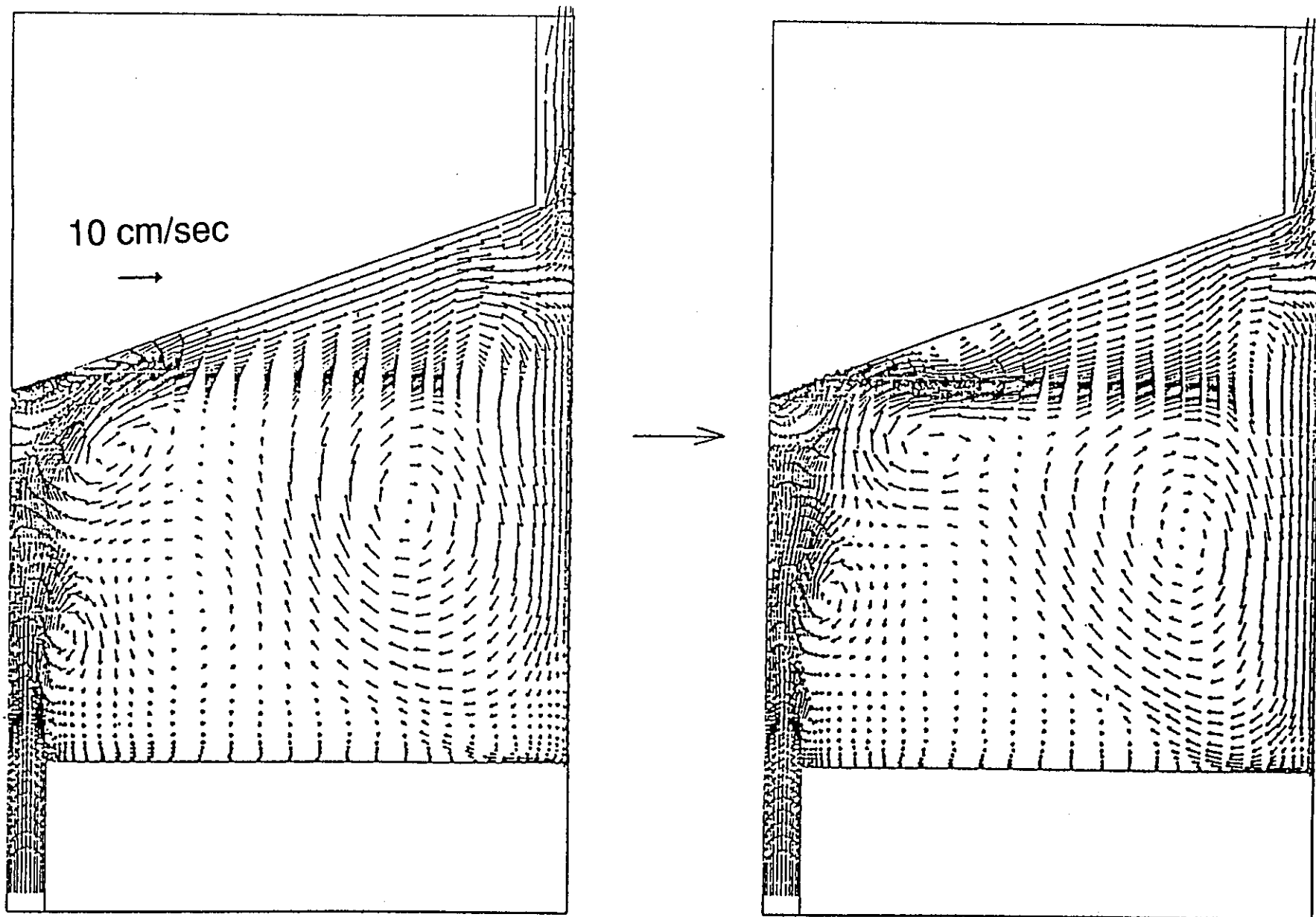
Fig. 22(b)　Calculated Velocity Vector Field in Case 4 by Method-DL3S
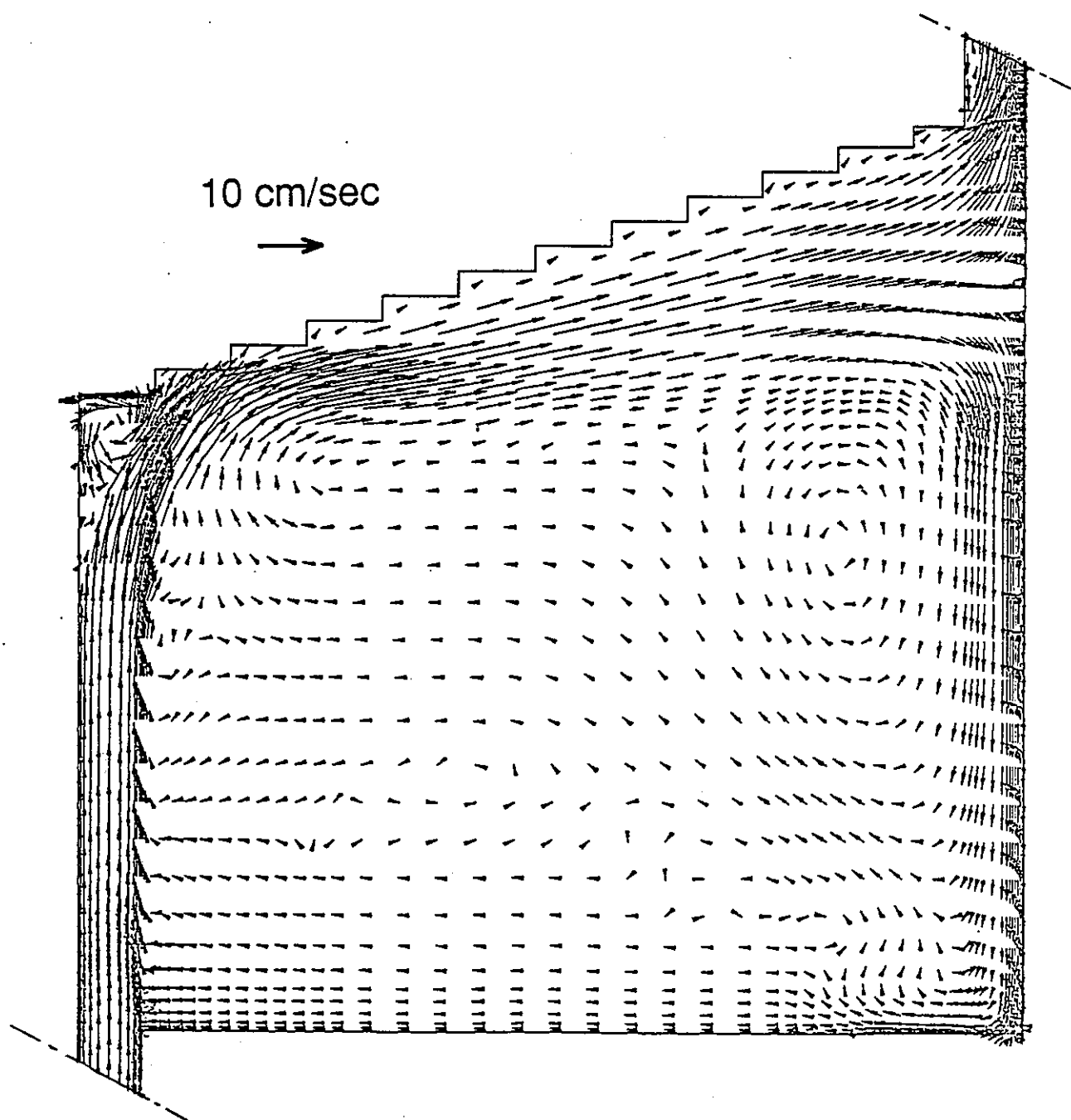
Fig. 22(c)   Calculated Velocity Vector Field in Case 4 by Method-DKQ
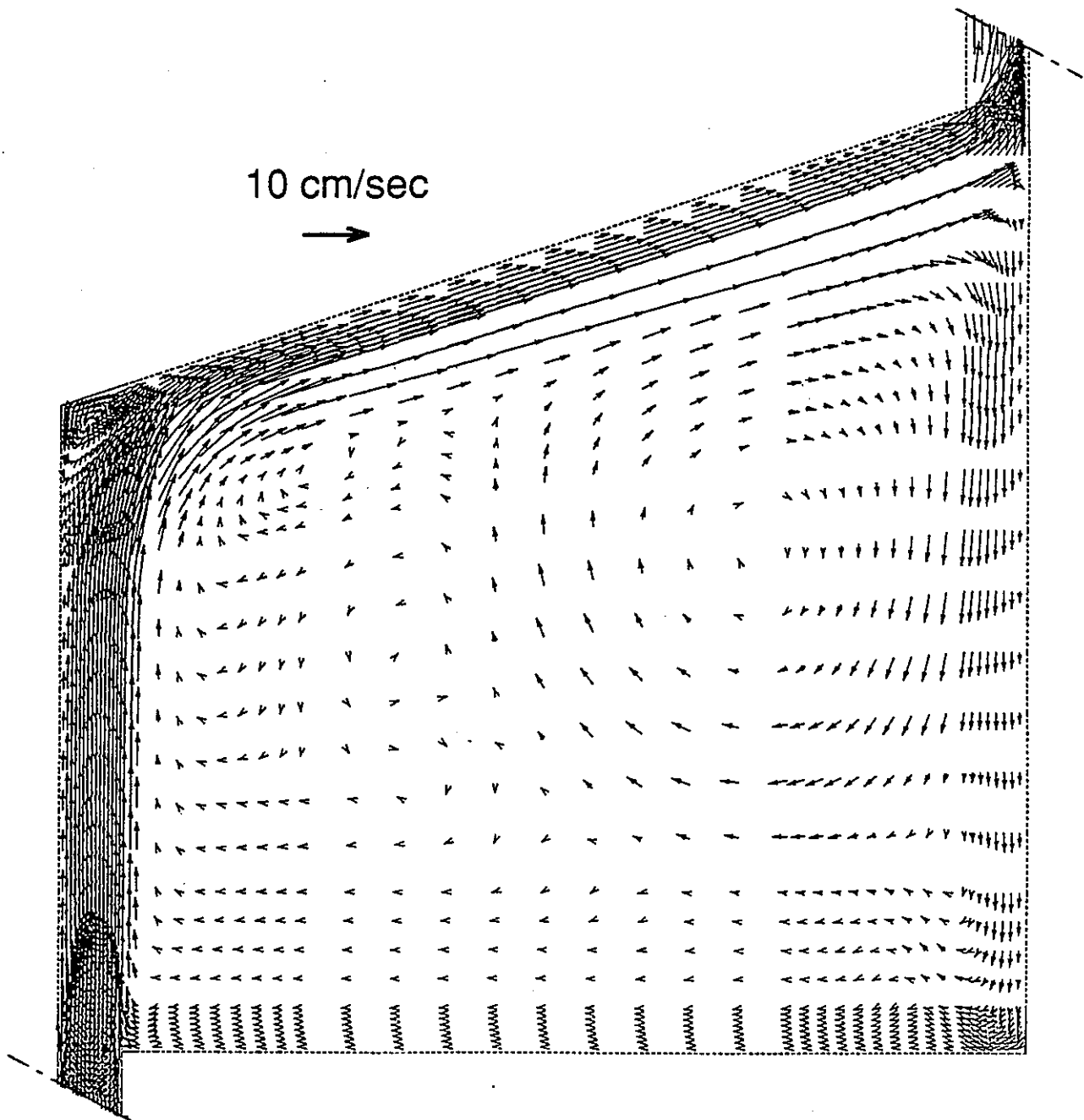
Fig. 22(d)   Calculated Velocity Vector Field in Case 4 by Method-EH

10 cm/sec
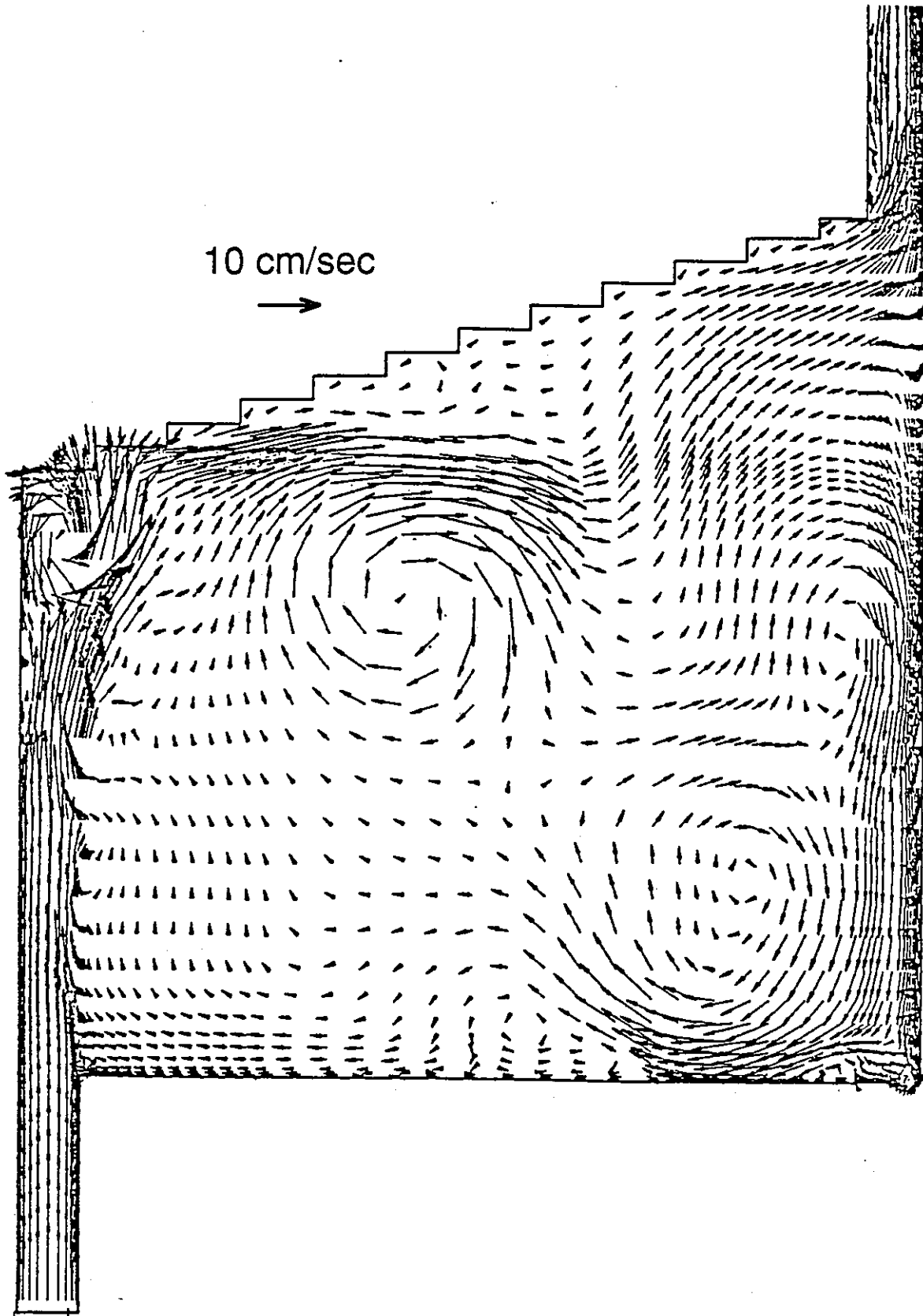
Fig. 23 Calculated Velocity Vector Field in Case 4 by a Finite
Difference Method with Laminar Model and QUICK Scheme
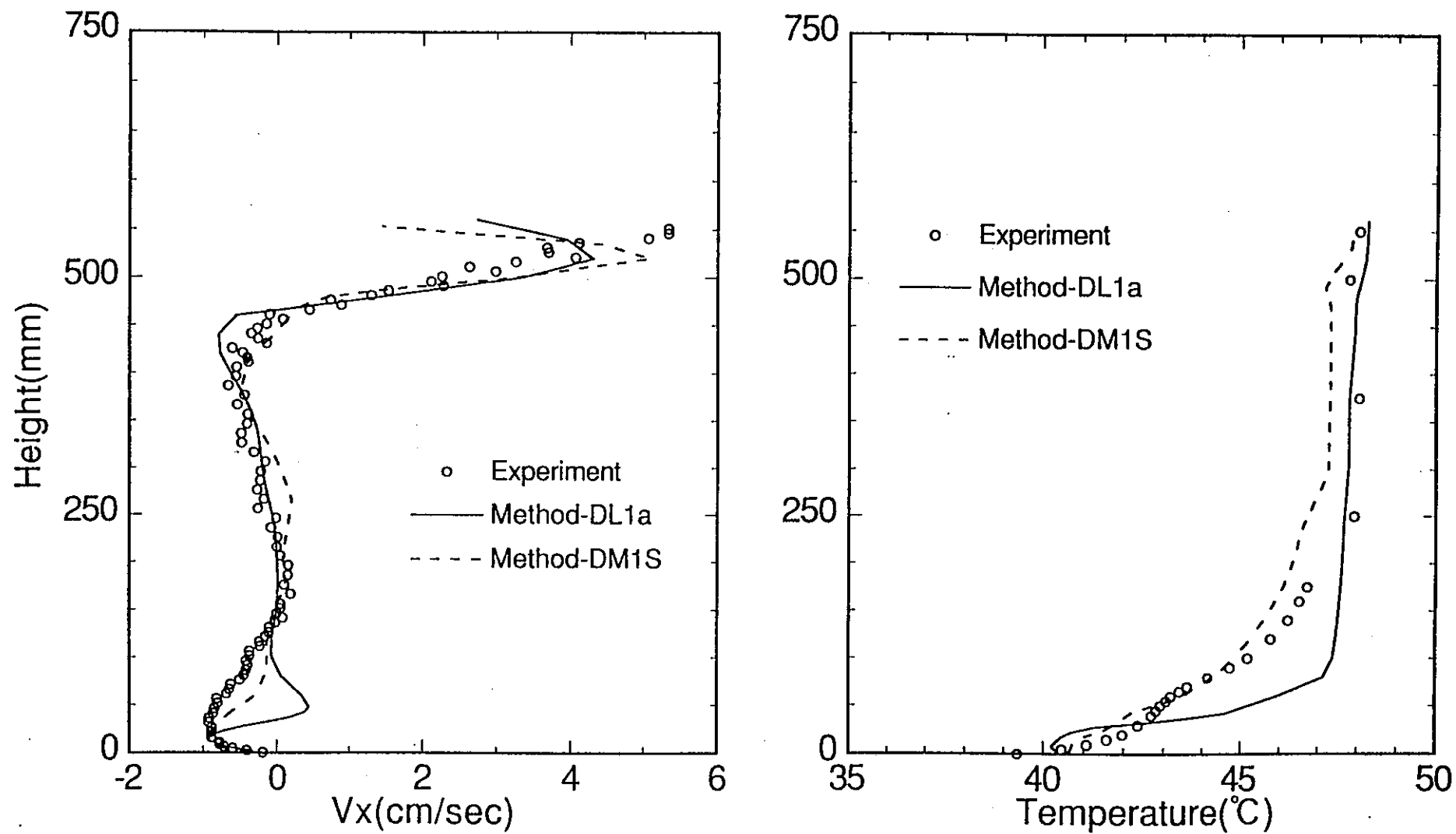
Fig. 24 Comparison of Stratified Flow Characteristics between
Method-DL1a and DM1S along P1 Line in Case 1
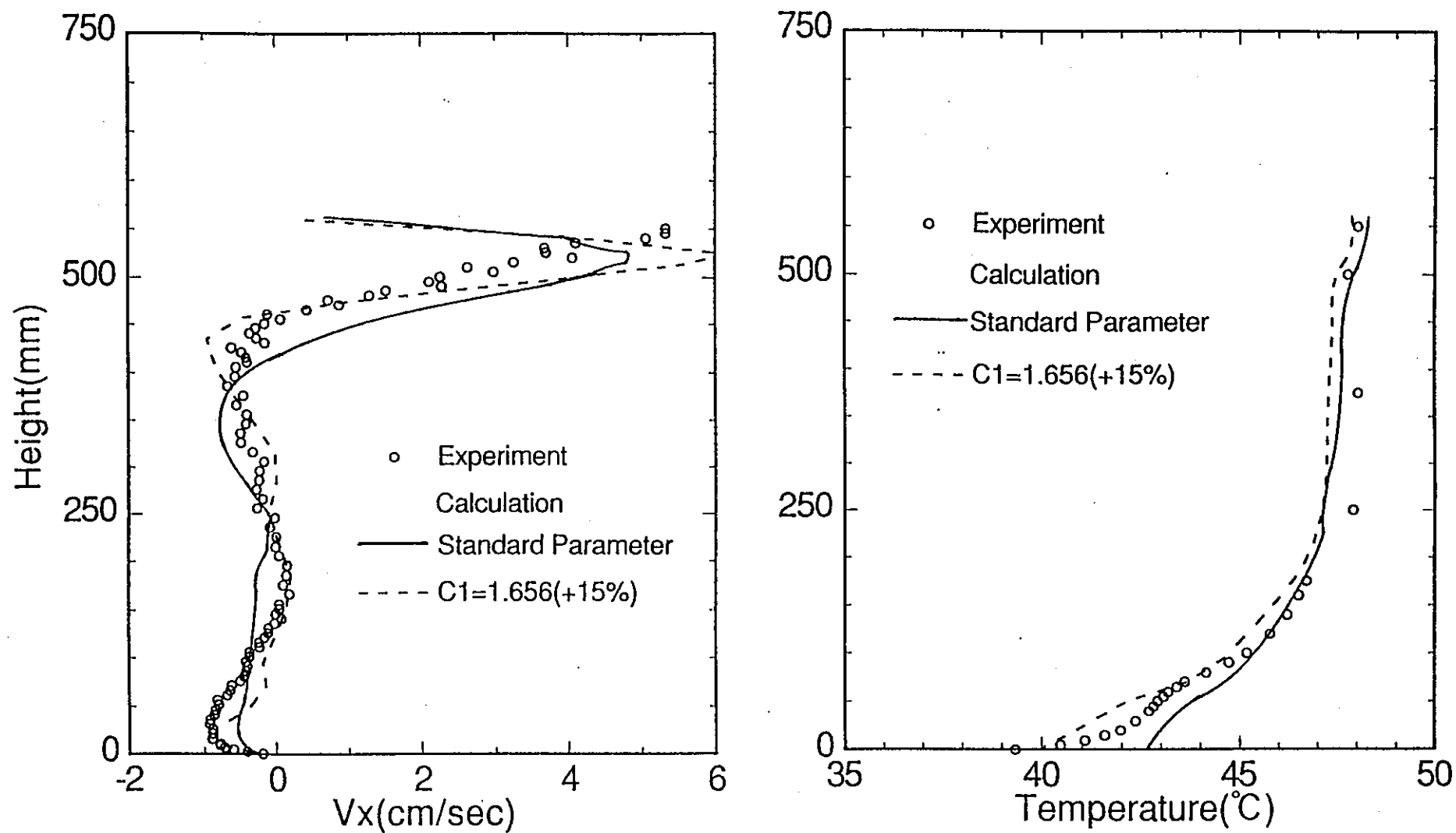
Fig. 25 Effect of Constant C1 of k-ε Turbulence Model on Velocity and
Temperature Distribution along P1 Line in Case 1
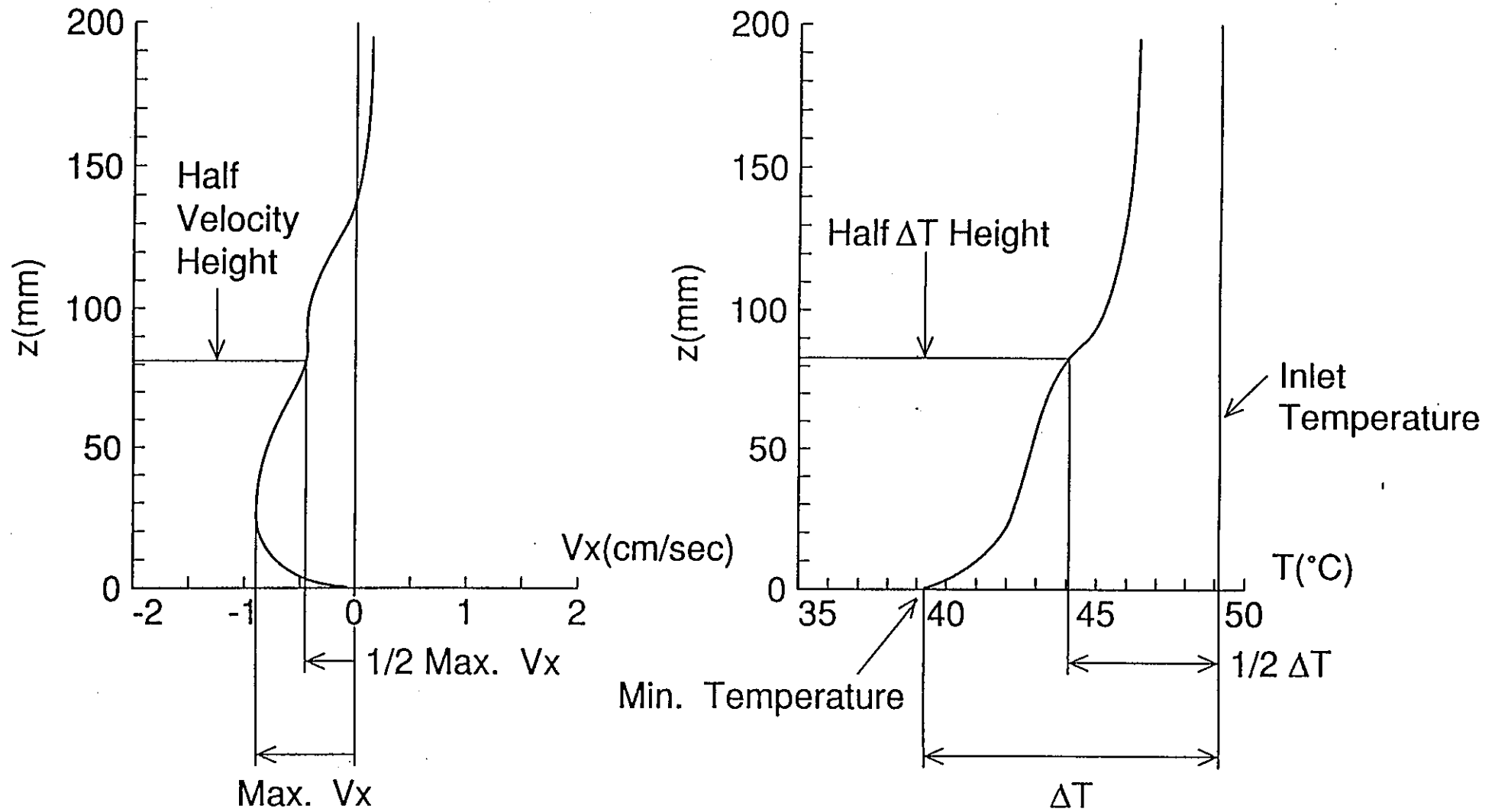
Fig.26 Characteristic Points of Stratified Flow along P1 Line
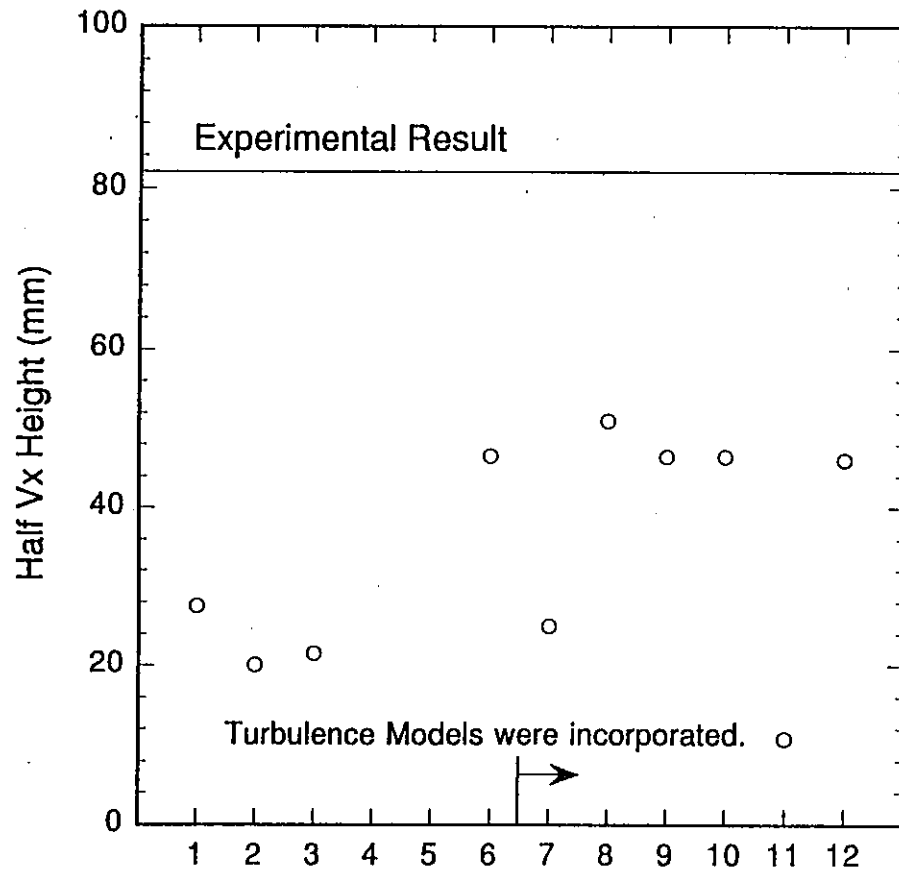
Half Velocity Height of Stratified Flow
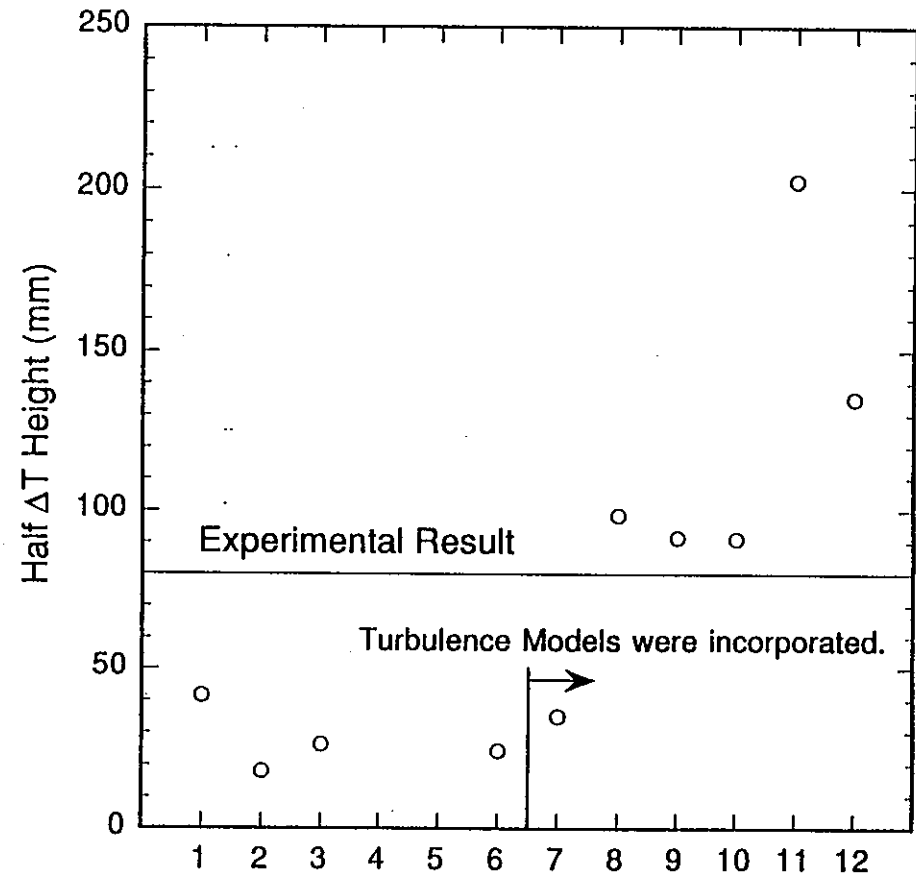
Half ΔT Height of Stratification Layer

Fig. 27   Comparison of Stratified Flow Characteristics among All
applied Methods in Case 1
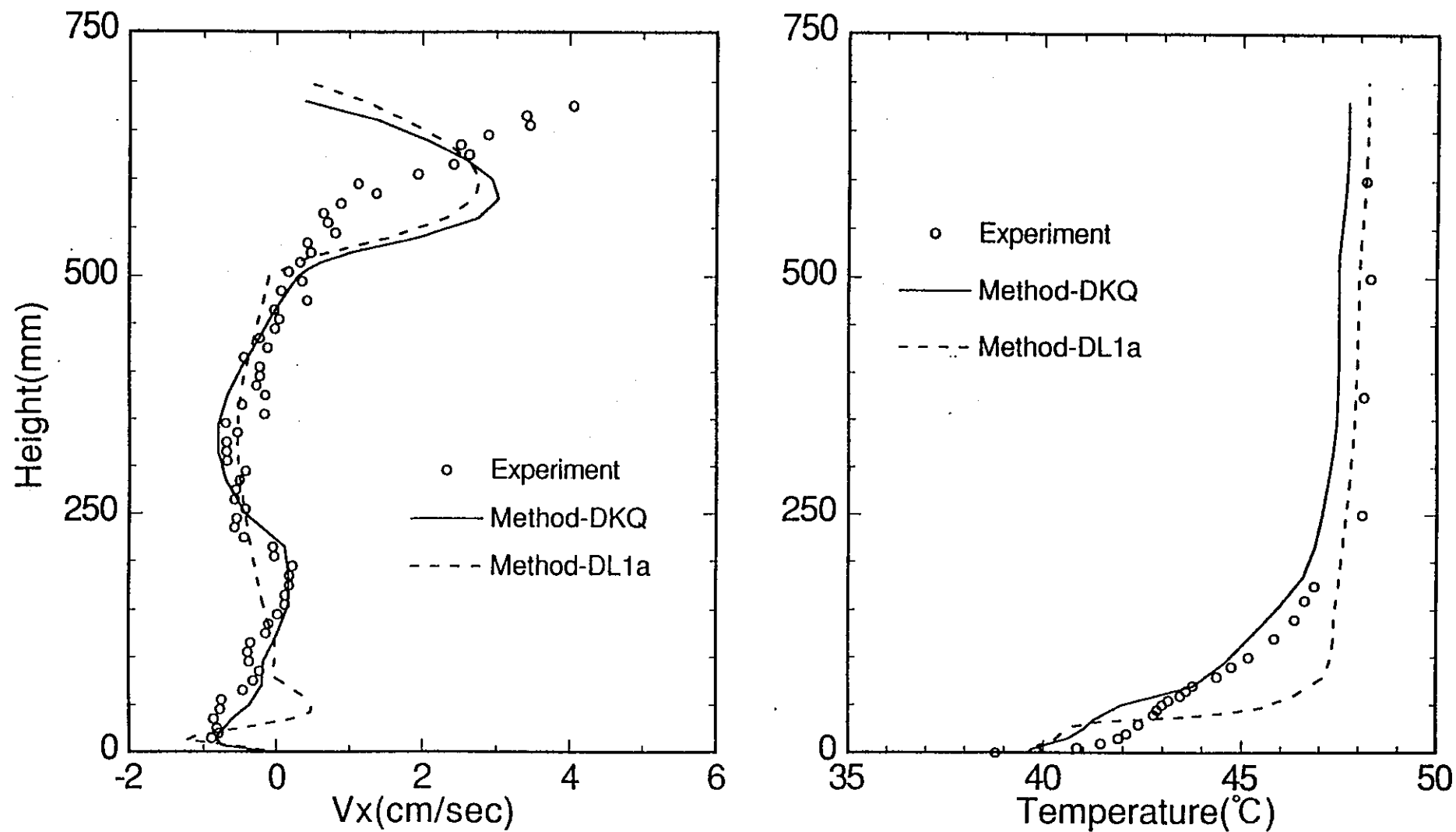
Fig. 28   Comparison of Recirculating Flow Characteristics between
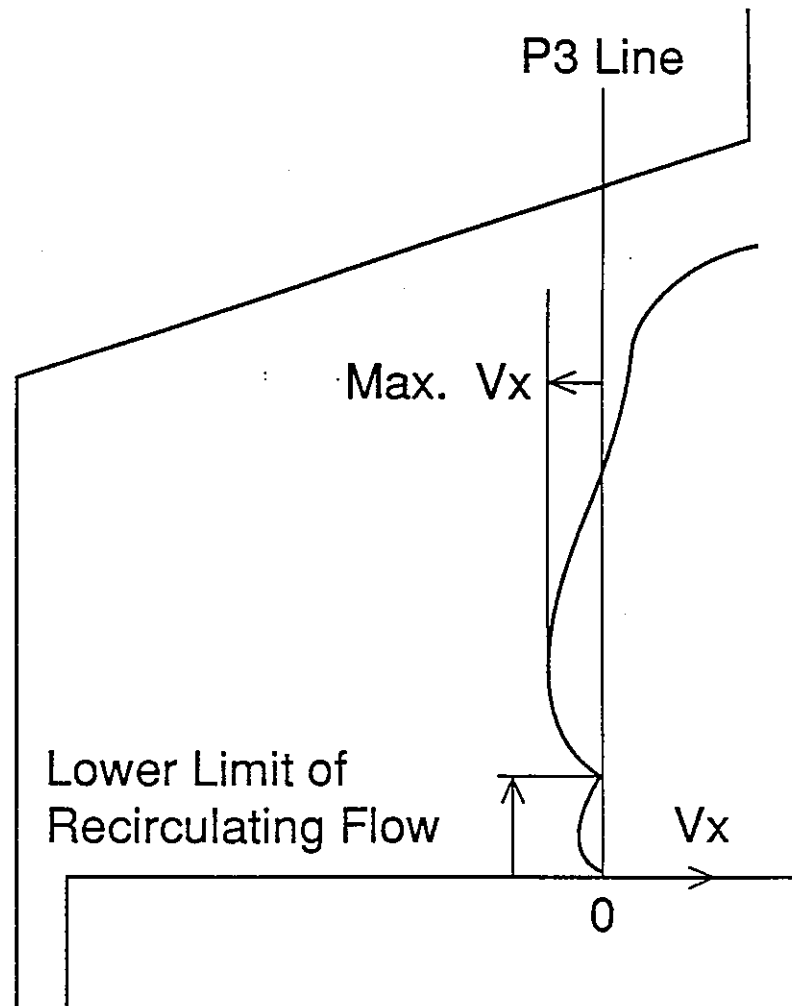Method-DL1a and DKQ along P3 Line in Case 1
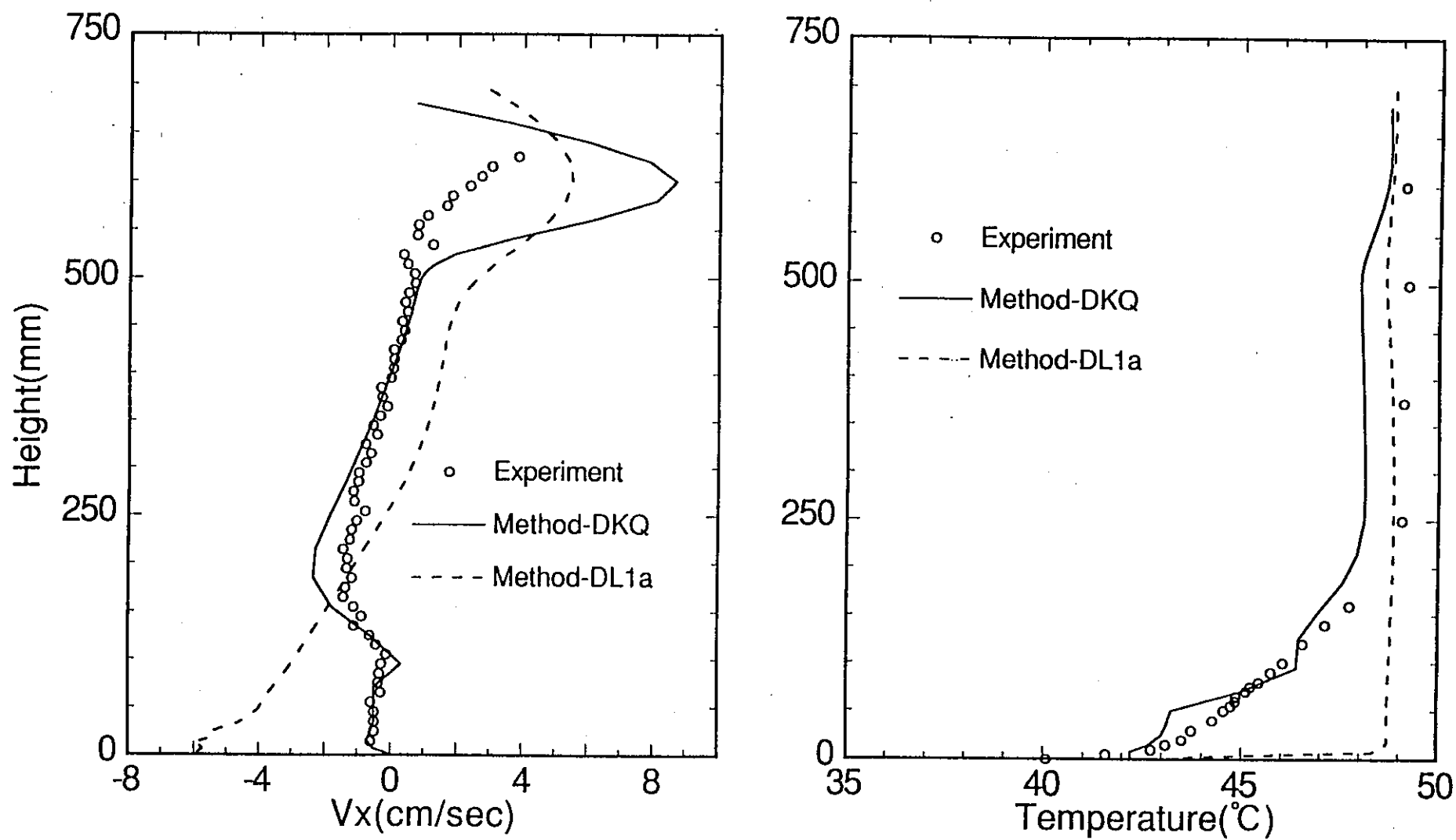
Fig. 29   Comparison of Recirculating Flow Characteristics between
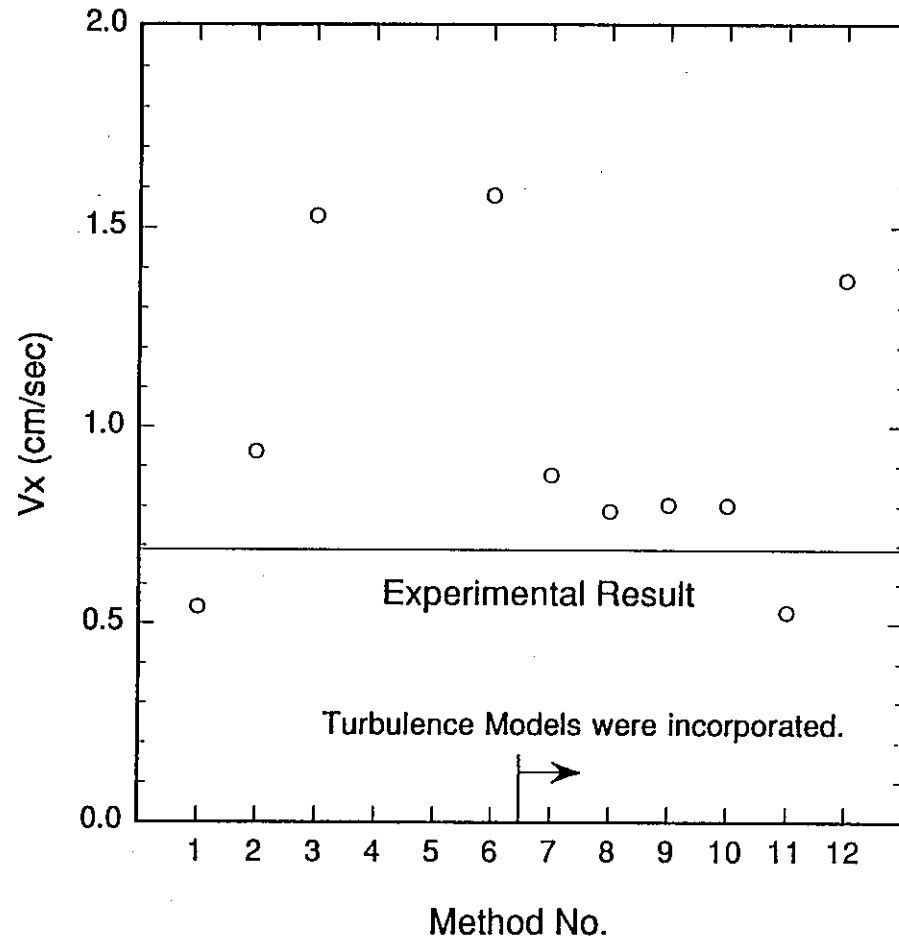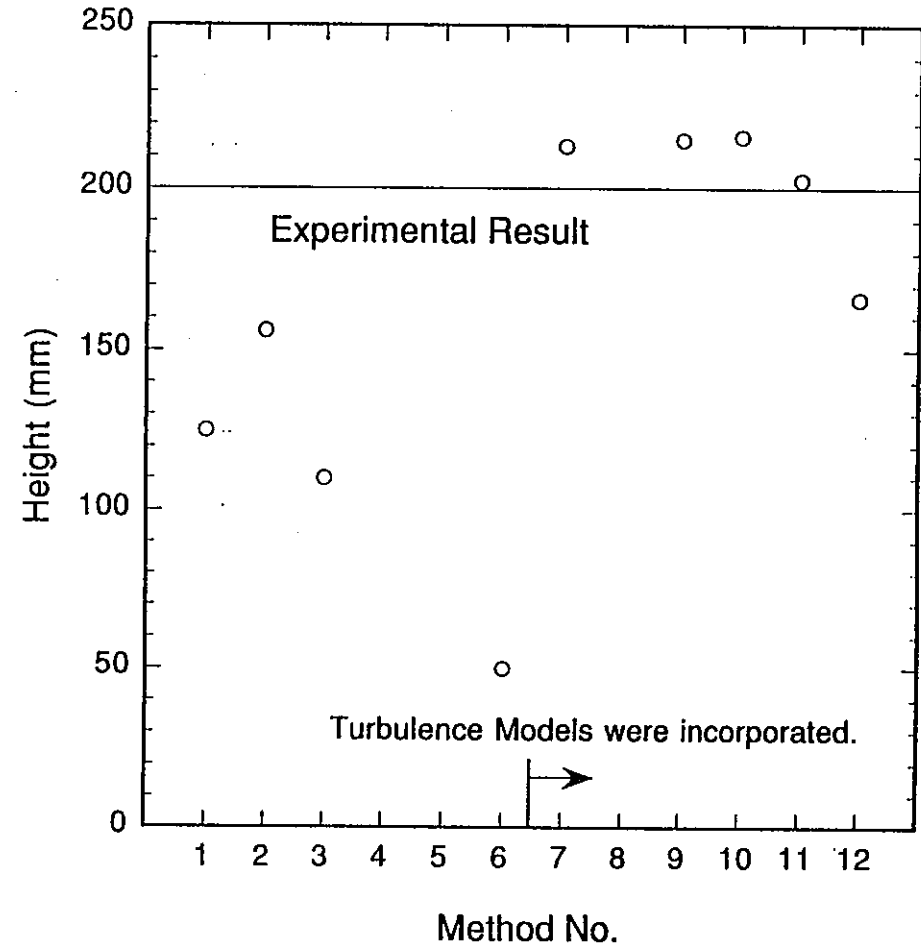Method-DL1a and DKQ along P3 Line in Case 4

Fig.30 Characteristic Points of Recirculating Flow along P3 Line
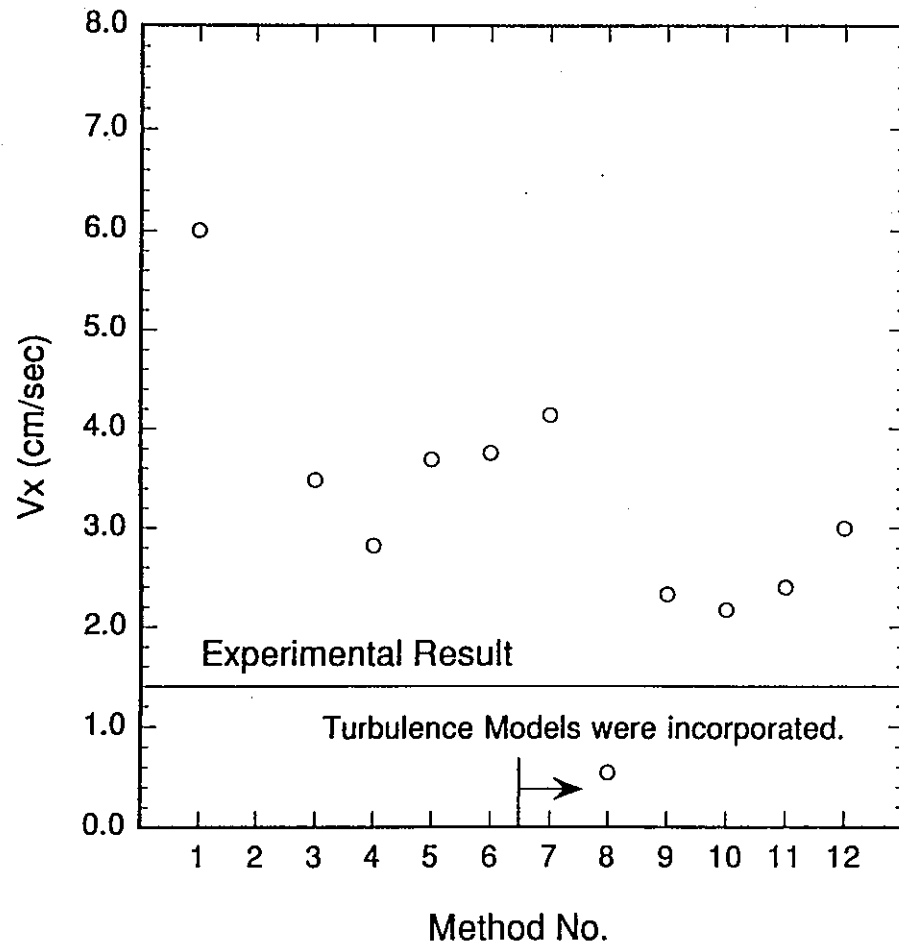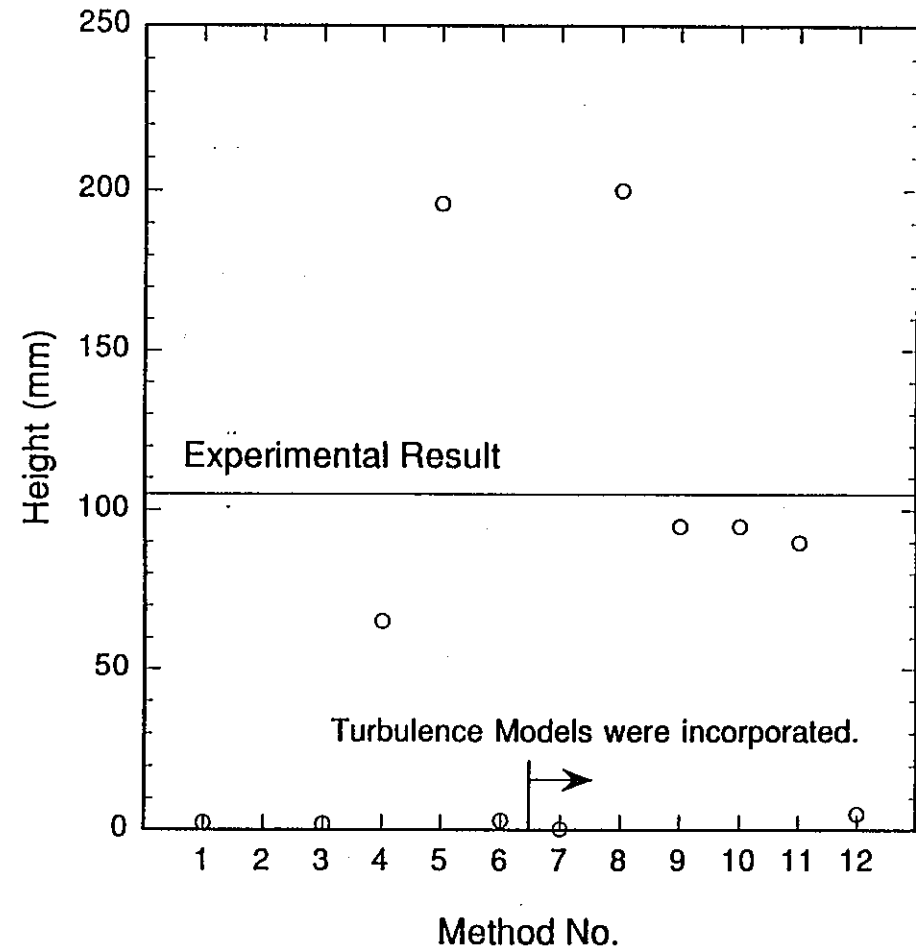
Maximum Vx of Recirculation flow

Lower Height of Recirculation Region

Fig. 31   Comparison of Recirculating Flow Characteristics among All
applied Methods in Case 1

Maximum Vx of Recirculation flow

Lower Height of Recirculation Region

Fig. 32   Comparison of Recirculating Flow Characteristics among All
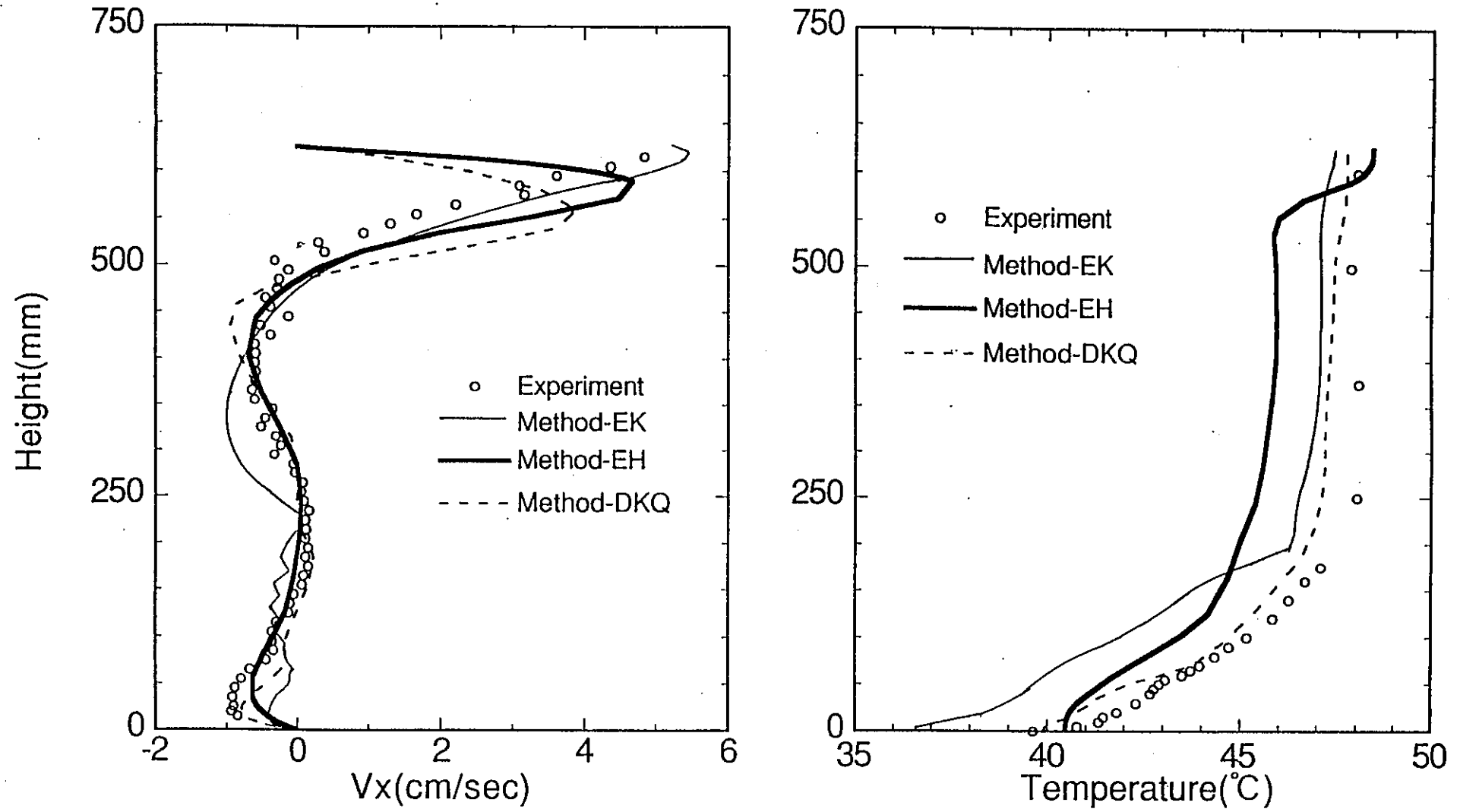applied Methods in Case 4

Fig. 33 Comparison of Flow Velocity near the Inclined Top Wall between Method-DKQ, -EH and Method-EK along P2 Line in Case 1
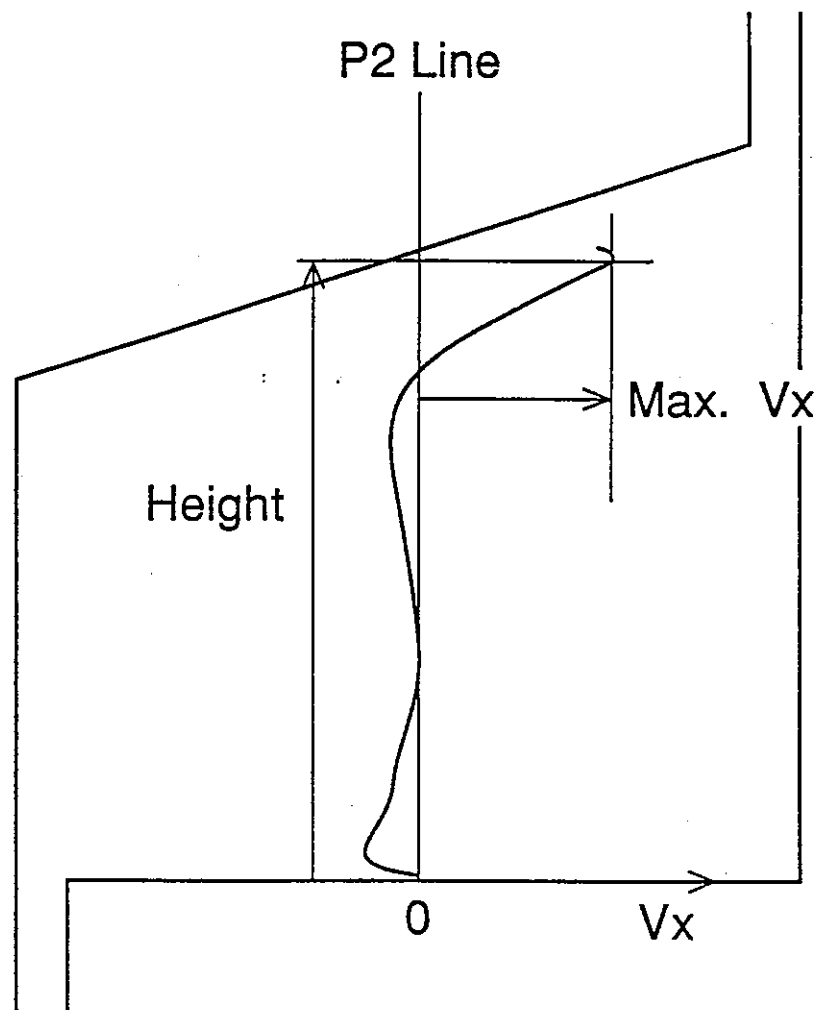
Fig. 34 Characteristic Points of Flow near the Inclined
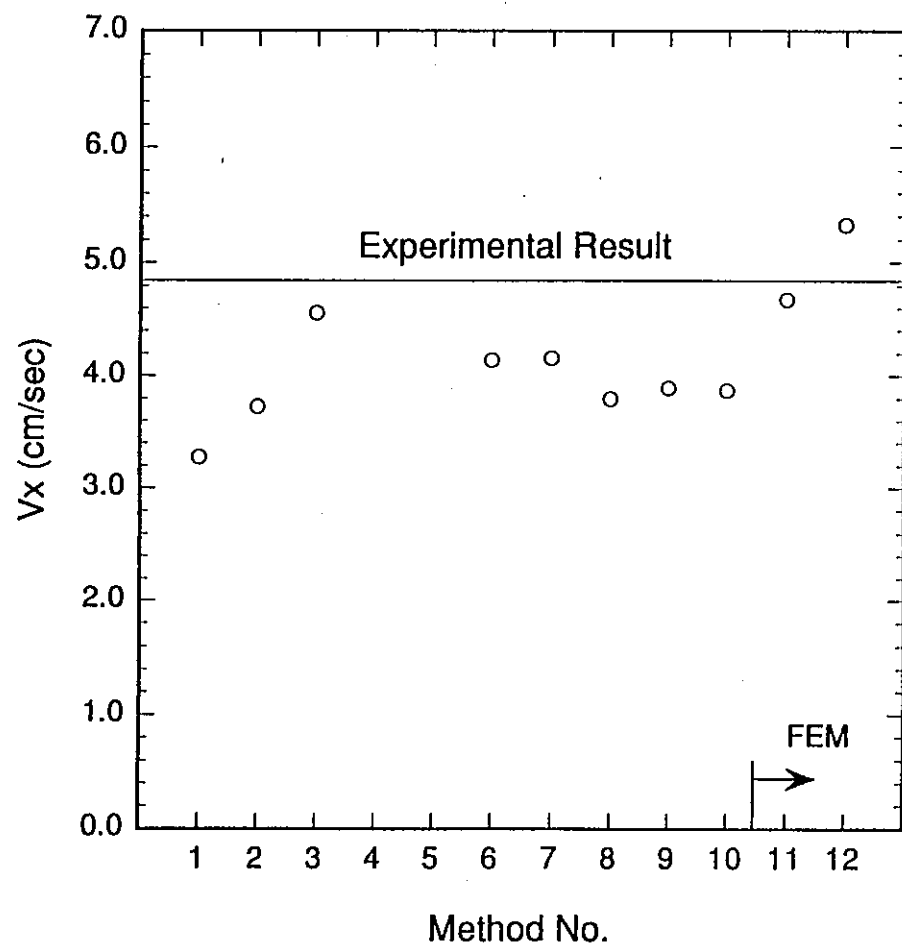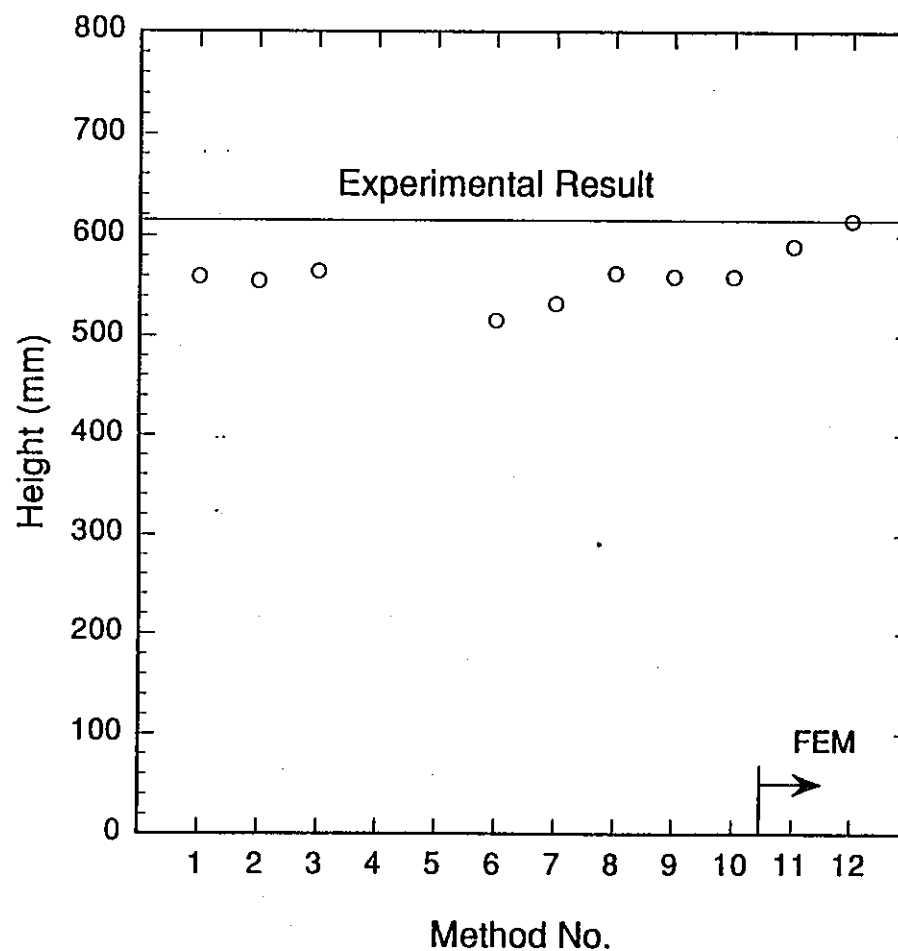Top Wall along P2 Line

Maximum Vx of Flow along the Inclined Wall

Height of Maximum Vx Position

Fig. 35   Comparison of Flow near the Inclined Top wall among All
applied Methods in Case 1

Sampling Time : 10 sec
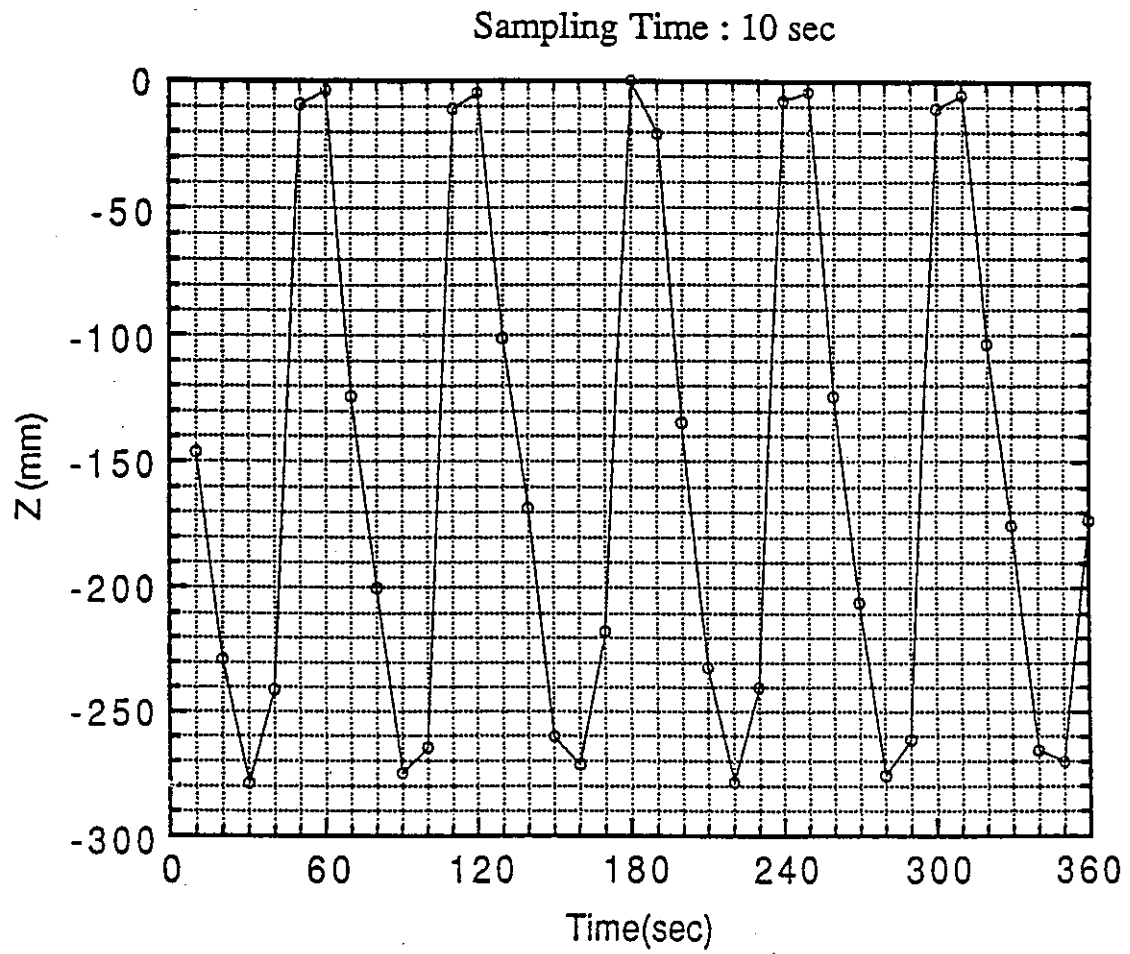

Fig. 36 Time Trace of Penetration Depth calculated by Method-DL1b
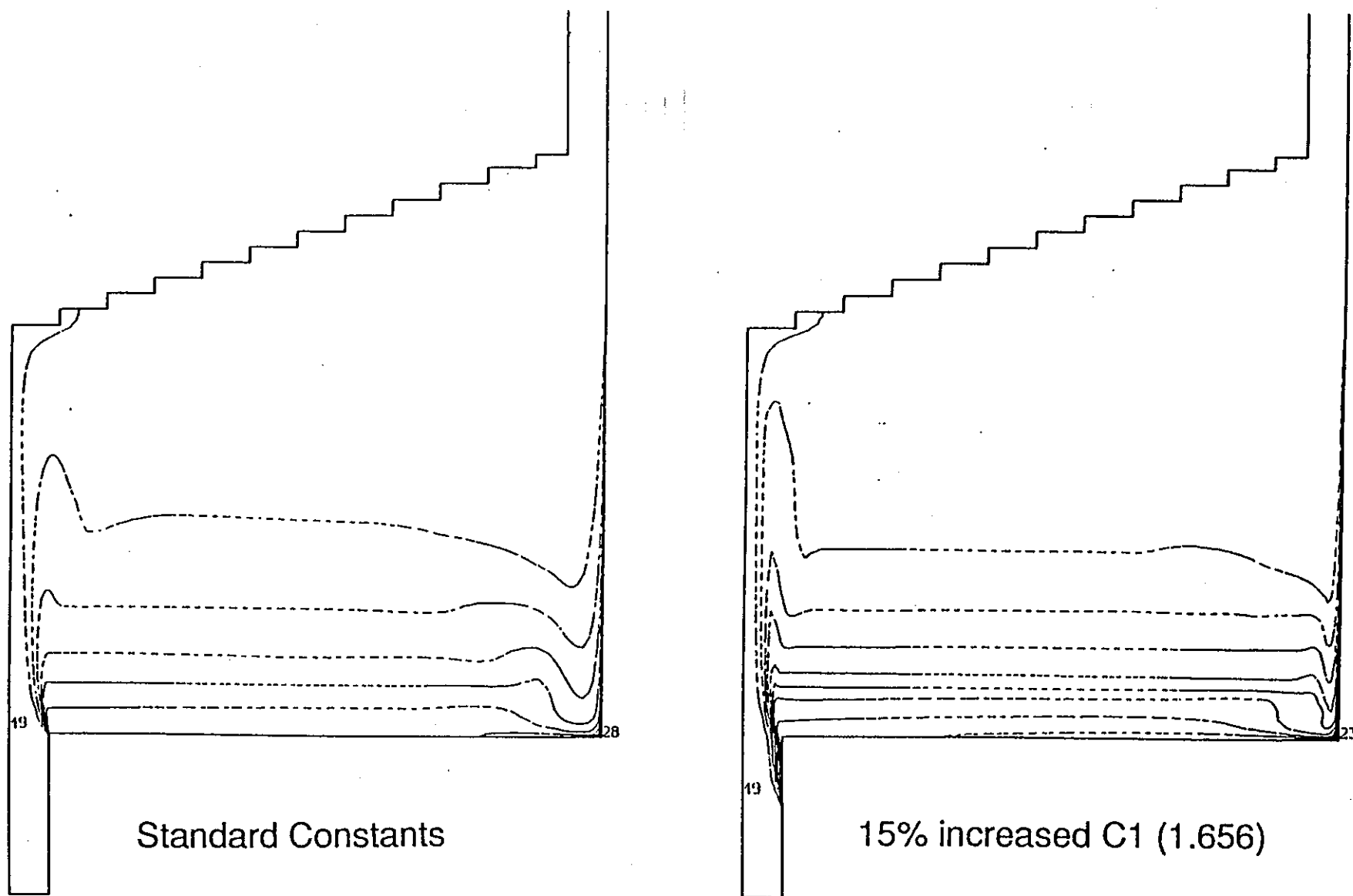
Standard Constants

15% increased C1 (1.656)

Fig. 37 Effect of Constant C1 of k-ε Turbulence Model on Temperature
Contour in the Plenum and Inlet Channel in Case 1

Appendix-1　Mixing length model incorporated in Method-DM1S

A turbulence model with zero equation based on the mixing length hypothesis was used. This model was applied to where boundary layer was observed in a preliminary calculation with a laminar model; adjacent to all walls in the plenum and inside of the inlet channel except for the inclined top wall.

Shear stress on the wall
The log law wall function was applied to calculate the shear stress on the wall.
For $y^+ > 12$,

$$\tau_w = \frac{\kappa u \mu y^+}{y \ln(9.0 \, y^+)} \tag{1}.$$

For $y^+ \leq 12$,

$$\tau_w = \mu \frac{\partial u}{\partial y} \tag{2}.$$

Where

    y^+ : Non-dimensional distance from the wall,

          $y^+ = u^* \, y \,/v$ (3),

    u^* : Friction velocity,

          $u^* = \tau_w \,/\rho$ (4),

    u : Velocity component parallel to the wall,

    y : Distance from the wall,

    κ : von Karman constant (= 0.6; recommended for wall jet),

    μ : Viscosity,

    v : Kinematic viscosity,

    ρ : Density,

    τ_w : Shear stress on the wall.

Mixing length model
Mixing length model was used to take account of turbulence momentum and heat fluxes, i.e.

$$u_i' \, u_j' = v_{eff} \frac{\partial u}{\partial y} \tag{5},$$

$$u_i' \, \phi' = \frac{v_{eff}}{Pr_t} \frac{\partial \phi}{\partial y} \tag{6}.$$

Where

    $u_i' \, u_j'$: Turbulence momentum flux $\times \, 1/\rho$,

    $u_i'\phi'$: Turbulence scalar flux $\times \, 1/\rho$,

    v_{eff} : Effective viscosity,

$$v_{eff} = v + l_m^2 \frac{\partial u}{\partial y} \tag{7},$$

    l_m : Mixing length,
    Pr_t : Turbulence Prandtl number (= 0.5),

    ϕ : Scalar contaminant.

The boundary layer on the wall of the plenum was treated as that of wall jet, while the inlet channel was treated as a pipe flow. Applied mixing length models are as follows.

(1) Mixing length model for the plenum wall boundary layer
a) Inner layer ($0 < y/\delta < \lambda/\kappa$)
The van Driest's hypothesis was applied to this region.

$$l_m = \kappa y \left[1.0 - \exp(-\frac{y^+}{26.0}) \right] \tag{8},$$

where

λ : Mixing length constant (= 0.075; recommended for the wall jet),

δ : Distance from the wall to the point where the velocity component parallel to the wall equals half of the maximum velocity nearby the wall.

b) Outer layer ($\lambda/\kappa < y/\delta$)

$$l_m = \lambda \delta \tag{9}.$$

(2) Mixing length model for the inlet channel
The Nikuradse's formula was chosen as an inlet channel turbulence model.

$$l_m = b [0.14 - 0.08 (1.0 - y/b)^2 - 0.06 (1.0 - y/b)^4] \tag{10},$$

where

b   : Half width of the inlet channel.

Appendix-2 Modification of a constant of k-ε model

k-ε model incorporated in Method-DKQ solvest the following transport equations of kinetic energy and its dissipation rate:

$$\frac{\partial}{\partial t}(\rho k) + \frac{\partial}{\partial x_i}(\rho U_i k) = \frac{\partial}{\partial x_i}(\frac{\mu_{eff}}{\sigma_k}\frac{\partial k}{\partial x_i}) + P + G - \rho\varepsilon$$

$$\frac{\partial}{\partial t}(\rho\varepsilon) + \frac{\partial}{\partial x_i}(\rho U_i\varepsilon) = \frac{\partial}{\partial x_i}(\frac{\mu_{eff}}{\sigma_\varepsilon}\frac{\partial\varepsilon}{\partial x_i}) + C_1\frac{\varepsilon}{k}(P + G)(1 - C_3\frac{G}{P+G}) - C_2\frac{\varepsilon^2}{k}$$

with

$$P = \mu_t\frac{\partial U_i}{\partial x_j}(\frac{\partial U_j}{\partial x_i} + \frac{\partial U_i}{\partial x_j})$$

$$G = g_i\beta\frac{\mu_t}{Pr_t}\frac{\partial T}{\partial x_i}$$

$$\mu_{eff} = \mu_l + \mu_t$$

$$\mu_t = \rho C_\mu\frac{k^2}{\varepsilon}$$

In the above modeling, the standard constants are as follows:

σ_k	σ_ε	C_1	C_2	C_3	C_μ	Pr_t
1.0	1.3	1.44	1.92	0.70	0.09	0.9

To apply low Re number flows like this benchmark problem, a sensitivity study of the model constants was carried out for a thermal cavity problem with air, which was investigated experimentally and numerically by Marie-Pierre Franklin, et.al.[10]. The model constant, C_1, was modified in the sensitivity study on the point that C_1 is a coefficient for the term including a buoyancy effect. The thermal cavity is illustrated in Fig. A1, which was in two dimension. The mean Nu number on the hot wall obtained from the sensitivity study is compared with the reference value of the Franklin et.al. in Fig. A2. From this study C_1 was defined as 1.656 (increased by 15% from the standard value, 1.44) for low Re flows.
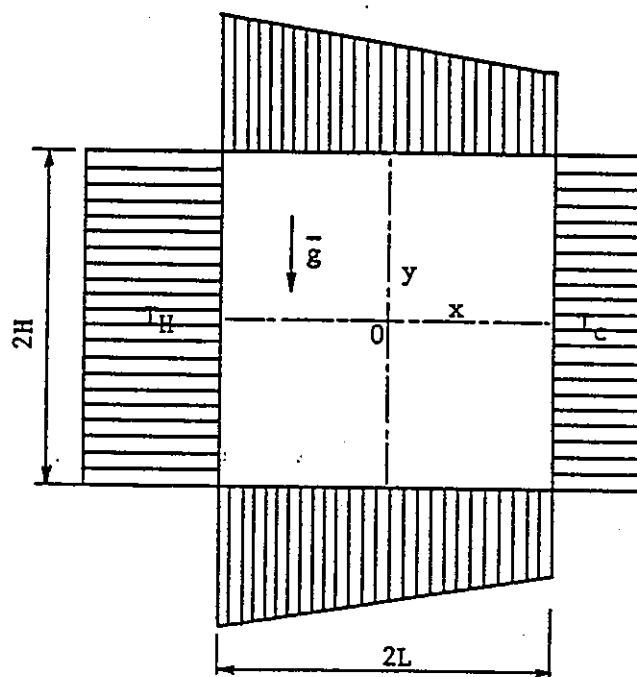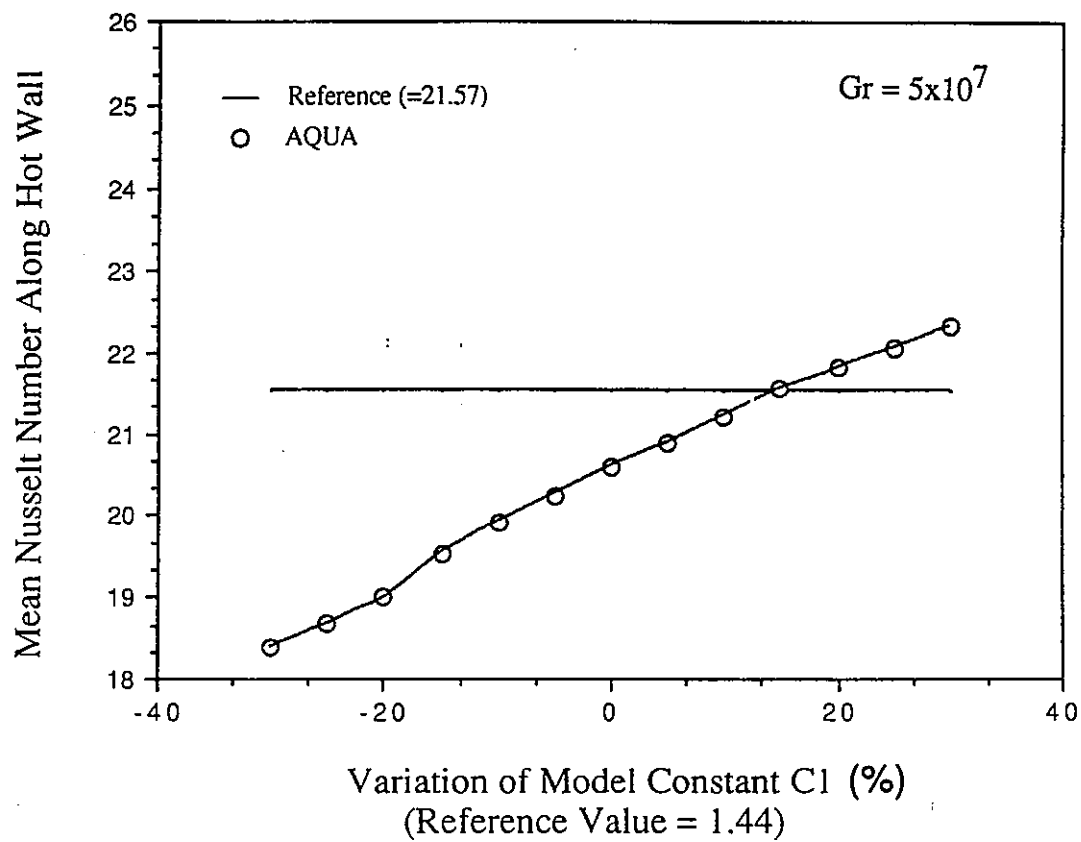
Fig. A1   Schematic of Thermal Cavity

Fig. A2 Effect of C_1 on Averaged Nu number along Hot Wall